On the role of dynamic stress concentrations and fracture mechanics in the longitudinal tensile failure of fibre-reinforced composites

Gianmaria Bullegas[a], Jorge Moledo Lamela[a,b], Soraia Pimenta[c], Silvestre T. Pinho[a]

[a] *Department of Aeronautics, Imperial College London, South Kensington Campus, SW7 2AZ London, United Kingdom*

[b] *School of Aeronautical and Space Engineering, Universidad Politecnica de Madrid, Plaza Cardenal Cisneros 3, 28040 Madrid, Spain*

[c] *Department of Mechanical Engineering, Imperial College London, South Kensington Campus, SW7 2AZ London, United Kingdom*

Abstract

This paper investigates the role of dynamic stress concentrations, and of fracture mechanics-driven growth of critical clusters of fibres, on the longitudinal tensile failure of fibre-reinforced composites. For this purpose, we developed a semi-analytical fibre bundle model to simulate the longitudinal tensile failure of large composite bundles of continuous fibres. The model uses shear-lag to calculate the stress recovery along broken fibres, and an efficient field superposition method to calculate the stress concentration on the intact fibres, which has been validated against analytical and Finite Element (FE) results from the literature.

The baseline version of the model uses static equilibrium stress states, and considers fibre failure driven by strength of materials (stress overload) as the only damage theory which can drive bundle failure. Like other models in the literature, the baseline model fails to capture the correct size effect (decreasing composite strength with bundle size) shown by experimental results.

Two model variants have been developed which include dynamics stress concentrations and a fracture mechanics failure criterion respectively. To the knowledge of the authors, it is the first attempt in the literature to investigate these two effects in a fibre bundle model by direct simulation of large composite bundles. It is shown that, although the dynamic stress concentration significantly decreases the predicted bundle strength, it does not allow to predict the correct trend of the size effect. Finally, the results suggest that fracture mechanics may be the physical mechanism which is necessary to include to correctly predict the decreasing composite strength with bundle size shown by experimental results.

Preprint submitted to Elsevier *January 26, 2020*

Keywords: Fibre Composites, Longitudinal Tensile Strength, Fracture Mechanics, Stress Concentrations, Micro-mechanics, Size Effects

---

Nomenclature

Roman Symbols

a_{cr}^{sj}	equivalent crack critical size
C_{sl}^{ij}	shear-lag boundary
E_1	composite tensile modulus
$e_{\bar{\mathrm{X}}}$	maximum accepted error on mean strength
G_{L}	energy release rate due to longitudinal crack propagation
G_{Lc}	critical energy release rates longitudinal crack propagation
G_{T}	energy release rate due to translaminar crack propagation
G_{Tc}	critical energy release rates for translaminar crack propagation
I_{cl}^{sj}	cluster criticality index
i	index across fibres
j	index across bundle sections
k	ndex across time steps
l_{el}	fibre element length
$l_{\mathrm{rl}}^{(ij)_{\mathrm{fa}}}$	recovery length associated with the failed fibre element $(ij)_{\mathrm{fa}}$
l_{s}	bundle length
m	shape parameters of Weibull strength distribution
N	number of Monte Carlo simulations

$\mathbb{N}_{\mathrm{fa}}$	set of failed elements in the bundle
$\mathbb{N}^{j}_{\mathrm{in}}$	set of intact elements in section j
$\mathbb{N}^{j}_{\mathrm{st}}$	set of elements that have reached the strain limit in section j
$\mathbb{N}^{j}_{\mathrm{st}}$	set of the saturated elements in section j
$\mathbb{N}^{j}_{\mathrm{in}}$	set of the intact elements in section j
$\mathbb{N}^{s}_{\mathrm{cl}}$	set of fibre elements in cluster s
$\mathbb{N}^{sj}_{\mathrm{cl}}$	set of neighbouring fibre elements associated with the cluster s in section j
n_{cl}	number of clusters in the bundle
$n^{(ij)^{s}_{\mathrm{cl}}}_{\mathrm{el,in}}$	number of intact neighbours of each element $(ij)^{s}_{\mathrm{cl}}$ of the cluster
$n^{ij}_{\mathrm{el,in}}$	number of intact neighbours of the element ij
n_{el}	total number of fibre elements in the bundle
n_{f}	total number of fibres in the bundle
n_{sec}	total number of bundle cross-sections
$r^{(ij)_{\mathrm{in}}(ij)_{\mathrm{st}}}$	distance between fibre elements in the cross section
$R^{ij}(t^{k})$	reserve factor used to calculate stress increase during failure simulation process
S_{L}	longitudinal finite width correction factor
S_{T}	translaminar finite width correction factor
s	index across the number of clusters in the bundle
SD_{b}	standard deviation of Normal strength distribution for bundle strength
t^{k}	time variable
V_{f}	fibre volume fraction
$w^{95\%}_{\mathrm{CI}}$	confidence interval at 95%

$X_0^{l_{\mathrm{el}}}$	scale parameter of Weibull strength distribution for a fibre element of length l_{el}
$X_0^{l_{\mathrm{r}}}$	scale parameter of Weibull strength distribution for a fibre with reference length l_{r}
X_{b}	bundle strength for each Monte Carlo simulation
X^{ij}	fibre element strength threshold assigned at the beginning of each Monte Carlo simulation
$\bar{X}_{\mathrm{b}}$	mean of the Normal strength distribution for bundle strength
x, y and z	coordinate reference system aligned with the bundle cross section and axis respectively

Greek Symbols

γ	parameter that controls the shape of the stress redistribution function
$\Delta t_{\mathrm{dyn}}^{k}$	transient interval for dynamic wave propagation
$\Delta\sigma^{(ij)_{\mathrm{in}}(ij)_{\mathrm{st}}}$	stress transferred from failed fibres to intact fibres
ε_{∞}	asymptotic strain
λ_{dyn}	dynamic magnification factor
λ_{fm}	proportionality factor in cluster criticality
μ_{12}	composite in plane shear modulus
σ_{∞}	asymptotic stress
σ_{dyn}	dynamic stress field
$\sigma_{\mathrm{eq}}^{sj}$	Equivalent stress for crack propagation
$\sigma_{\mathrm{po}}^{sj}$	average pull-out stress
$\sigma_{\mathrm{sl}}^{ij}$	shear-lag stress limit
$\sigma^{(ij)}$	longitudinal stress in fibre element ij
τ_{fr}	friction stress
τ_{sl}	yielding stress

ϕ_f	fibre diameter

Acronyms

FE	Finite Element
FRP	Fibre Reinforced Plastic
GLS	Global Load Sharing
LLS	Local Load Sharing
Model BA	Baseline model version
Model DE	Model including Dynamic Effects
Model FM	Model including Fracture Mechanics effects
UC	Unit Cells
UD	Uni-Directional
WLT	Weakest Link Theory
WOW	Weibull of Weibull

1. Introduction

The strength and stiffness of Fibre Reinforced Plastic (FRP) laminates is controlled, to a great extent, by the fibres in the load-aligned plies, thus fibre-dominated tensile failures (also known as translaminar failures) can lead to a significant drop in local stiffness, and can trigger catastrophic failure of an entire composite structure. Consequently, being able to accurately characterise and predict the longitudinal tensile strength of Uni-Directional (UD) FRP plies is of great importance. The longitudinal tensile strength of UD composites is characterised by strong size effects connected to both the length of the specimens and the total number of fibres [1–4]. Although manufacturing and testing artefacts may influence the results and interfere with measured size effects, most researchers agree that size effects in composites are due to the intrinsic properties and failure mechanisms of the material [1].

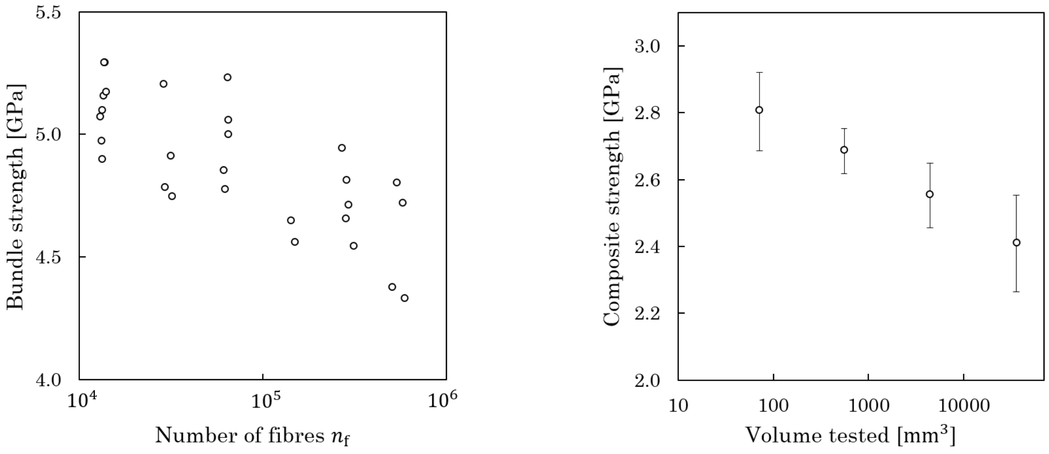

(a) (b)

Figure 1: Size effects in the longitudinal tensile strength of UD carbon-epoxy composites. (a) Size effect in the strength of composite bundles of constant length but different filament counts [5]. (b) Size effect in the strength of scaled UD composites measured in tapered specimens especially designed to fail in the gauge section and avoid gripping effects [6].

The final failure of FRPs under longitudinal tensile stress is governed by the formation of clusters of broken fibres which, once reaching a critical size, can evolve catastrophically. Since the nucleation of these clusters is usually triggered by the presence of defects in the fibres (weak fibres), a larger composite structure (with more and/or longer fibres than a smaller one) will be more likely to have more and larger defects, which will make the formation of a critical cluster of broken fibres more likely. Fig. 1 shows two examples of size effects on the longitudinal tensile failure of UD carbon-epoxy specimens [5, 6].

Size effects pose a challenge for the design of large composite structures based on experimental data measured from small coupons, and quantifying them through predictive models has been the subject of a recent blind benchmark exercise [7] where most models failed to predict size effects and formation of clusters of broken fibres accurately.

A UD FRP bundle is typically composed of millions of individual fibres all aligned in the same direction and bound together by the matrix. The longitudinal tensile failure process is governed at least in part by the stochastic variability of the single fibre strength, and by the stress redistribution that occurs around broken fibres [8–14]. Predicting the tensile strength accurately at the macro-scale requires the ability to take into account at least both these micro-mechanical effects. To this end, several Fibre Bundle Models (FBMs) have been developed in the literature.

FBMs typically consider a parallel array of fibres with stochastic strength, loaded remotely under tension (bundle stress σ_∞ and strain ε_∞) [5, 15–29]. Once the weakest fibre fails, this generates a stress concentration in the neighbouring intact fibres, potentially leading to their failure. Remote tensile stresses or strains are progressively increased until all fibres are broken, or until the composite cannot withstand further load increments. In general, the ultimate strength of the bundle is a stochastic variable which has to be characterised statistically by the modelling results.

The problem of calculating the probability distributions of bundle strength can be approached analytically, or through Monte Carlo simulations. Analytical FBMs are typically classified depending on the load sharing in the neighbourhood of a fibre break: Global (or Equal) Load Sharing (GLS or ELS) models consider the same stress concentration on all non-broken fibres [15–17]; Local Load Sharing (LLS) models assume that the closest neighbours to the broken fibre undergo higher stress concentrations than the more distant ones [18–20]. Pimenta and Pinho [29] recently proposed an analytical hierarchical scaling law for the strength of composite fibre bundles which has been extensively validated against experimental results [7], and predicts full strength distributions of bundles with millions of fibres in less than 1 second.

Monte Carlo FBMs proposed in the literature can be broadly classified into two categories depending on the method used to calculate the stress field around broken fibres [8]:

- Finite Element (FE) methods, which use full-field FE solvers [19–25] or simplified spring-based models [5, 26, 27, 30] to calculate the stress field in the bundle. Full-field FE models can be further subdivided in single-scale models, which simulate the stress field in the entire bundle at each step of the Monte Carlo simulations process [19–22]; and two-scales models, which use FE to calculate the deterministic response of Unit Cells (UCs) with different numbers of fibre breaks, and then use those responses in Monte Carlo simulations [23–25]. A main drawback with FE Monte Carlo simulations is computational efficiency, as a very fine mesh of fibre elements and a large number of simulations are required to achieve representative results.

- Combined field-superposition methods, which calculate deterministic stress fields near single-fibre breaks at a first stage, and then use a superposition method to include those fields in the failure simulations of fibre bundles with multiple breaks. The literature on this type of simulation is extensive, and most of the earlier models [10–14] considered analytical solutions for stress fields. More recently, Swolfs et al. [28] used FE simulations of UD composites (with realistic fibre packing) to calibrate an analytical stress redistribution function. For combined field-superposition methods, it is challenging to capture how stress concentrations and recovery lengths are affected by interacting clusters of broken fibres [22].

Despite attempting to simulate the micro-mechanical evolution of damage during the composite tensile failure, most Monte Carlo FBMs in the literature tend to overestimate the final bundle strength when compared with experimental data, and to underestimate the decrease in strength with the increasing number of fibres in the bundle (size effect) [5, 26–28].

Bazant [31] has shown that final failure of a composite structure is governed by the composite strength for small-scale components, and by the composite fracture toughness for large-scale components. Pimenta et al. and Henry et al. [32, 33] applied this concept to predict tensile failure of aligned discontinuous composites using a non-linear fracture mechanics criterion, which combines strength-dominated and toughness-dominated failure modes. However, most FBMs which use high-fidelity representation of the failure process only consider fibre stress overload (i.e. a strength of materials approach) as the bundle failure criterion, and do not include fracture mechanics based failure criteria for the growth of larger clusters of broken fibres. This is an important observation as there is growing experimental evidence that unstable failure of a carbon fibre/polymer matrix bundle occurs when a cluster of approximately 14 or more broken fibres is formed [34, 35] (Fig. 2). Furthermore, fibre failure is a dynamic process, resulting in a change in the stress field over time, before it finally dampens out to the static level. Dynamic stress concentrations can be significantly higher than static ones, as shown by modelling results [18, 36–39]. Nevertheless, this effect is typically ignored and only static equilibrium stress states are considered in all state-of-the-art FBMs [9].

In this work, we aim to investigate the role of dynamic effects, and of fracture mechanics-driven growth of clusters of broken fibres, in longitudinal failure. To this end, we developed an efficient Monte Carlo FBM with a semi-analytical field superposition method to calculate stress concentrations around clusters of broken fibres. The stress redistribution for single broken fibres and clusters has been validated against analytical and FE results from the literature [22]; the method is also able to capture analytically the dependency of the stress recovery length on the cluster size.

The Monte Carlo simulation process was optimised using statistical analysis to allow the direct

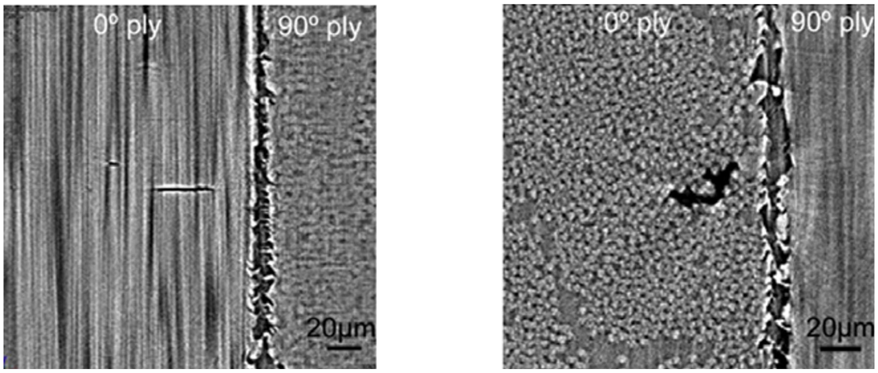

(a) (b)

Figure 2: Computer tomography image of a co-planar cluster of 14 fibre breaks [35]. (a) Side view. (b) Top view.

simulations of large bundle sizes. Using this technique, it was possible to explore the size effects for large composite bundles by direct simulation, without relying on analytical extrapolation of the simulated results. Finally, this allowed us to investigate for the first time the effects of dynamic stress concentration and toughness dominated failure on the composite strength distribution and on the related size effects for large composite bundles. The code-base for the implementation of the model in a MATLAB® environment, along with the most important simulation results discussed in this paper, can be found in a publicly available repository on GitHub.com [40].

This document is organised as follows. Section 2 explains the baseline model and its variants (including the model geometry, how damage is simulated and the post-processing of the data). The algorithms required for the numerical implementation are listed in Section 2.5. Section 3 contains an overview of the numerical results and a comparison between experimental and predicted strength distributions both in micro and macro-bundles. Finally, Section 4 draws the main conclusions.

2. Model development

2.1. Introduction

This section describes in detail the development of the baseline version of the model (referred to as model BA) which considers static equilibrium stress states, and uses strength of materials as the only failure theory. Two model variants including dynamic effects and fracture mechanics effects are presented in Sections 2.3 and 2.4 respectively. To achieve a reliable comparison of the results, all models share the same common structure described once for model BA in Section 2.2.

2.2. Baseline model

Model BA simulates the failure of a bundle of parallel fibres under longitudinal tensile loading and provides the statistical distribution for the ultimate bundle strength. The simulation strategy can be broken down into three main components:

- Model definition: the numerical, geometrical and mechanical properties need to be defined, and a stochastic strength distribution needs to be assigned to the fibres. This is described in Section 2.2.1.
- Failure simulation: an asymptotic stress $\sigma_\infty(t^k)$, which is a function of the time variable t^k, is applied to the bundle to drive the failure process. When a fibre element breaks/fails as a consequence of this load, the broken fibre element is unable to carry the asymptotic stress, which needs to be redistributed on the surrounding fibres. The stress redistribution is computed in three steps: (i) calculation of the stress transferred by shear-lag along the broken fibre, (ii) redistribution of the load on the surviving intact fibres, and (iii) verifying whether new fibre elements break due to stress overload and updating $\sigma_\infty(t^k)$ to advance the simulation. Steps (i), (ii) and (iii) are discussed in Sections 2.2.2, 2.2.3 and 2.2.4, respectively. This procedure is repeated until final failure of the bundle.
- Post-processing: at the end of the failure simulation, the final value of the bundle strength X_b is obtained, being equal to the maximum of $\sigma_\infty(t^k)$ recorded during the simulation. Then, the process is repeated over different realisations of the initial stochastic assignment of the fibre strength in a Monte Carlo simulation, and the parameters of the bundle strength distribution are extracted. This simulation is optimised as described in Section 2.2.5 to achieve computational efficiency for very large bundles while ensuring the reliability and validity of the results.

2.2.1. Bundle geometry and fibre strength

Fig. 3 shows a bundle of n_f fibres of length l_s and diameter ϕ_f, with fibre volume fraction V_f and inter-fibre spacing s in the x and y directions. Each fibre in the bundle is subdivided into smaller fibre elements of size l_el, therefore creating n_sec cross sections j with $j = 1, ..., n_\mathrm{sec}$ in the bundle along the direction z, each one containing fibre elements i with $i = 1, ..., n_\mathrm{f}$. The indices i, j therefore define each of the $n_\mathrm{el} = n_\mathrm{f} \times n_\mathrm{sec}$ fibre elements in the bundle.

The bundle is loaded in tension by the asymptotic stress $\sigma_\infty(t^k)$ applied to the fibres extremities. The current version of the model assumes that the fibres are packed in a square arrangement, as it has been established that the differences in strength predictions due to fibre arrangements are remarkably small [13, 41].

To model the stochastic variability of the fibre strength, a strength value X^{ij} is assigned to each fibre element following a Weibull distribution [42] with failure probability F_el:

$$F_\mathrm{el}(X^{ij}) = 1 - \exp\left(-\frac{X^{ij}}{X_0^{l_\mathrm{el}}}\right)^m, \tag{1}$$

where $X_0^{l_\mathrm{el}}$ is the scale parameter of the strength distribution for a fibre element of length l_el, and can be determined using the Weakest Link Theory (WLT) [8, 43]:

$$X_0^{l_\mathrm{el}} = X_0^{l_\mathrm{r}} \left(\frac{l_\mathrm{r}}{l_\mathrm{el}}\right)^{1/m}, \tag{2}$$

where $X_0^{l_\mathrm{r}}$ and m are the scale and shape parameters respectively for a single fibre with reference length l_r. The Weibull distribution is widely adopted in the literature [22, 26–29, 44–49], considering the generally good correlation with single fibre tests [50, 51]. However, other authors have proposed alternative distributions, e.g. Bimodal Weibull or Weibull of Weibull distributions [5, 52–54].

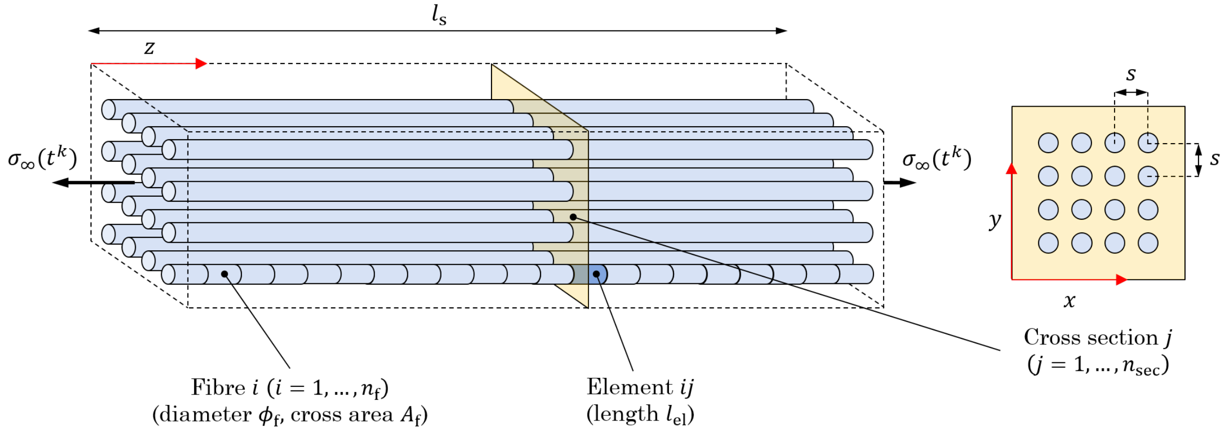

Figure 3: Description of the model geometry.

2.2.2. Shear-lag stress limit and recovery length

At each step t^k of the simulation[1], it is possible to define the set $\mathbb{N}_{\mathrm{fa}}$ of failed elements in the bundle. For each broken fibre i with a failed element $(ij)_{\mathrm{fa}}$, the longitudinal stress in that element goes to zero ($\sigma^{(ij)_{\mathrm{fa}}} = 0$), but it is progressively recovered in the rest of the fibre due to the shear stress transmitted by the matrix via a shear-lag mechanism [15, 29, 55, 56].

Assuming that the axial load is only carried by the fibres, and that the matrix is loaded in shear to the yielding stress τ_{sl} (perfectly plastic behaviour), the shear-lag stress limit $\sigma_{\mathrm{sl}}^{(ij)(ij)_{\mathrm{fa}}}$ (maximum stress level allowed by the shear-lag stress recovery) for each element ij in fibre i due to the failed element $(ij)_{\mathrm{fa}}$ can be calculated applying force equilibrium:

$$\sigma_{\mathrm{sl}}^{(ij)(ij)_{\mathrm{fa}}} = \sum_{\mathbb{N}_{\mathrm{sl}}^{(ij)(ij)_{\mathrm{fa}}}} C_{\mathrm{sl}}^{ij} \cdot \frac{\tau_{\mathrm{sl}}}{A_{\mathrm{f}}} \cdot l_{\mathrm{el}} \ , \tag{3}$$

where $\mathbb{N}_{\mathrm{sl}}^{(ij)(ij)_{\mathrm{fa}}}$ is the set of fibre elements in fibre i contained between ij and $(ij)_{\mathrm{fa}}$, and C_{sl}^{ij} is the shear-lag boundary, which is the contour over which the shear stress is transmitted for each fibre element. The calculation of the shear-lag boundaries is detailed in Appendix A.1.

In the case of two or more failed elements in the same fibre, the shear-lag stress limit for each element in the fibre is the smallest one of those relative to the different breaks, hence:

$$\sigma_{\mathrm{sl}}^{ij} = \begin{cases} \infty & \text{if } \nexists\ (ij)_{\mathrm{fa}} \in \text{fibre } i; \\ \min\limits_{(ij)_{\mathrm{fa}}} \left(\sigma_{\mathrm{sl}}^{(ij)(ij)_{\mathrm{fa}}}\right) & \text{if } \exists\ (ij)_{\mathrm{fa}} \in \text{fibre } i. \end{cases} \tag{4}$$

The portion of the broken fibre i where $\sigma_{\mathrm{sl}}^{ij} \leq \sigma_{\infty}$ defines the recovery length $l_{\mathrm{rl}}^{(ij)_{\mathrm{fa}}}$ associated with the failed fibre element $(ij)_{\mathrm{fa}}$ (Fig. 4). The elements $(ij)_{\mathrm{st}}$ within a recovery length are considered to be *saturated* elements, since they reached the shear-lag limit. The remaining elements are *intact* elements.

When the recovery lengths associated with two or more failed elements belonging to neighbouring fibres overlap, the load transmission between the fibres is impeded along the overlapped length, thus the saturated elements within this length are considered to be part of the same cluster (Fig. 4a).

---

[1] for the brevity and clarity of notation, the dependency on the time variable t^k will be omitted through Sections 2.2.2 and 2.2.3

This consideration modifies the shear-lag boundary C_{sl}^{ij} for the involved elements and in consequence the shear-lag stress limit and the recovery length varies as well (Fig. 4b).

Therefore, the calculation of the shear-lag stress limit needs to be performed iteratively, as described in Appendix A.2. A functional description of the iterative steps to calculate the shear-lag stress limit is explained below:

(i) Eqs. (3)-(4) are applied considering that all the elements in the bundle are intact to obtain an initial condition for the shear-lag stress limit (hereafter *initial solution*) to start the iterative process.

(ii) The recovery lengths are calculated and the shear-lag boundaries are updated for the saturated elements.

(iii) Eqs. (3)-(4) are applied again to obtain a first solution for the shear-lag stress limit (hereafter *simplified shear-lag stress limit*).

(iv) Steps (ii) and (iii) are performed iteratively until convergence to determine the exact solution (hereafter *exact shear-lag stress limit*).

In order to understand the effect of the different proposed approaches of calculating the recovery length for clusters of broken fibres on the model results, three different versions of model BA are implemented and compared in this paper:

(i) model BA.1: the iterative process to calculate the shear-lag stress limit is stopped at the first step, thus the effect of clusters is not captured, the shear-lag boundaries are equal to the fibre circumference for each fibre element and the solution is the initial solution for the shear-lag stress limit;

(ii) model BA.2: the iterative process to calculate the shear-lag stress limit is stopped at the second step, thus the effect of clusters is captured in an approximate form and the solution is the simplified shear-lag stress limit.

(iii) model BA.3: the iterative process to calculate the shear-lag stress limit is carried out until converge, thus capturing the full effect of the clusters and the solution is the exact shear-lag stress limit.

The results of three models are presented and discussed in Section 3.1.1.

2.2.3. Stress redistribution

Once the shear-lag stress limit is defined for each fibre, the final stress state in the bundle is computed by redistributing the loss of stress from the broken fibres to the remaining intact fibres in the same cross section. At each bundle cross section j, it is possible to define the set $\mathbb{N}^j_{\mathrm{st}}$ of the saturated elements $(ij)_{\mathrm{st}}$ that reached the shear-lag limit ($\sigma_{\mathrm{sl}}^{(ij)_{\mathrm{st}}} \leq \sigma_\infty$), and the set $\mathbb{N}^j_{\mathrm{in}}$ of the intact elements $(ij)_{\mathrm{in}}$, for which $\sigma_{\mathrm{sl}}^{(ij)_{\mathrm{in}}} > \sigma_\infty$.

An analytical power law is used to efficiently compute the stress redistribution [22, 57]. The additional stress $\Delta\sigma^{(ij)_{\mathrm{in}}(ij)_{\mathrm{st}}}$ redistributed on the intact element $(ij)_{\mathrm{in}} \in \mathbb{N}^j_{\mathrm{in}}$ as a result of the stress loss on element $(ij)_{\mathrm{st}} \in \mathbb{N}^j_{\mathrm{st}}$ has the following expression:

$$\Delta\sigma^{(ij)_{\mathrm{in}}(ij)_{\mathrm{st}}} = \Phi^{(ij)_{\mathrm{st}}} \cdot \left(\frac{r^{(ij)_{\mathrm{in}}(ij)_{\mathrm{st}}}}{s}\right)^{-\gamma}, \tag{5}$$

where $r^{(ij)_{\mathrm{in}}(ij)_{\mathrm{st}}}$ is the distance between fibre elements in the cross section and is normalised by fibre spacing s (hereafter indicated with $\bar{r}^{(ij)_{\mathrm{in}}(ij)_{\mathrm{st}}}$), and γ is a parameter which controls the shape of the stress redistribution function. The variable $\Phi^{(ij)_{\mathrm{st}}}$ is calculated by imposing force equilibrium to the bundle cross section j:

$$\sigma_\infty - \sigma_{\mathrm{sl}}^{(ij)_{\mathrm{st}}} = \sum_{\mathbb{N}^j_{\mathrm{in}}} \Phi^{(ij)_{\mathrm{st}}} \cdot \left(\bar{r}^{(ij)_{\mathrm{in}}(ij)_{\mathrm{st}}}\right)^{-\gamma} \Rightarrow \Phi^{(ij)_{\mathrm{st}}} = \frac{\sigma_\infty - \sigma_{\mathrm{sl}}^{(ij)_{\mathrm{st}}}}{\sum\limits_{\mathbb{N}^j_{\mathrm{in}}} \left(\bar{r}^{(ij)_{\mathrm{in}}(ij)_{\mathrm{st}}}\right)^{-\gamma}}. \tag{6}$$

The final stress field at each bundle cross section is computed applying the principle of superposition of effects to the stress concentration generated by each saturated element:

$$\sigma^{ij} = \begin{cases} \sigma_{\mathrm{sl}}^{ij} & \text{if } ij \in \mathbb{N}^j_{\mathrm{st}}; \\ \sigma_\infty + \sum\limits_{\mathbb{N}^j_{\mathrm{st}}} \Delta\sigma^{(ij)_{\mathrm{in}}(ij)_{\mathrm{st}}} & \text{if } ij \in \mathbb{N}^j_{\mathrm{in}}. \end{cases} \tag{7}$$

As a consequence of the stress concentration, it may happen that new elements in the cross section reach their shear-lag limit ($\sigma_\infty + \sum\limits_{\mathbb{N}^j_{\mathrm{st}}} \Delta\sigma^{(ij)_{\mathrm{in}}(ij)_{\mathrm{st}}} > \sigma_{\mathrm{sl}}^{ij}$), and the excess stress has to be further redistributed. This is achieved by re-calculating the stress field using Eqs. (5) to (7) iteratively,

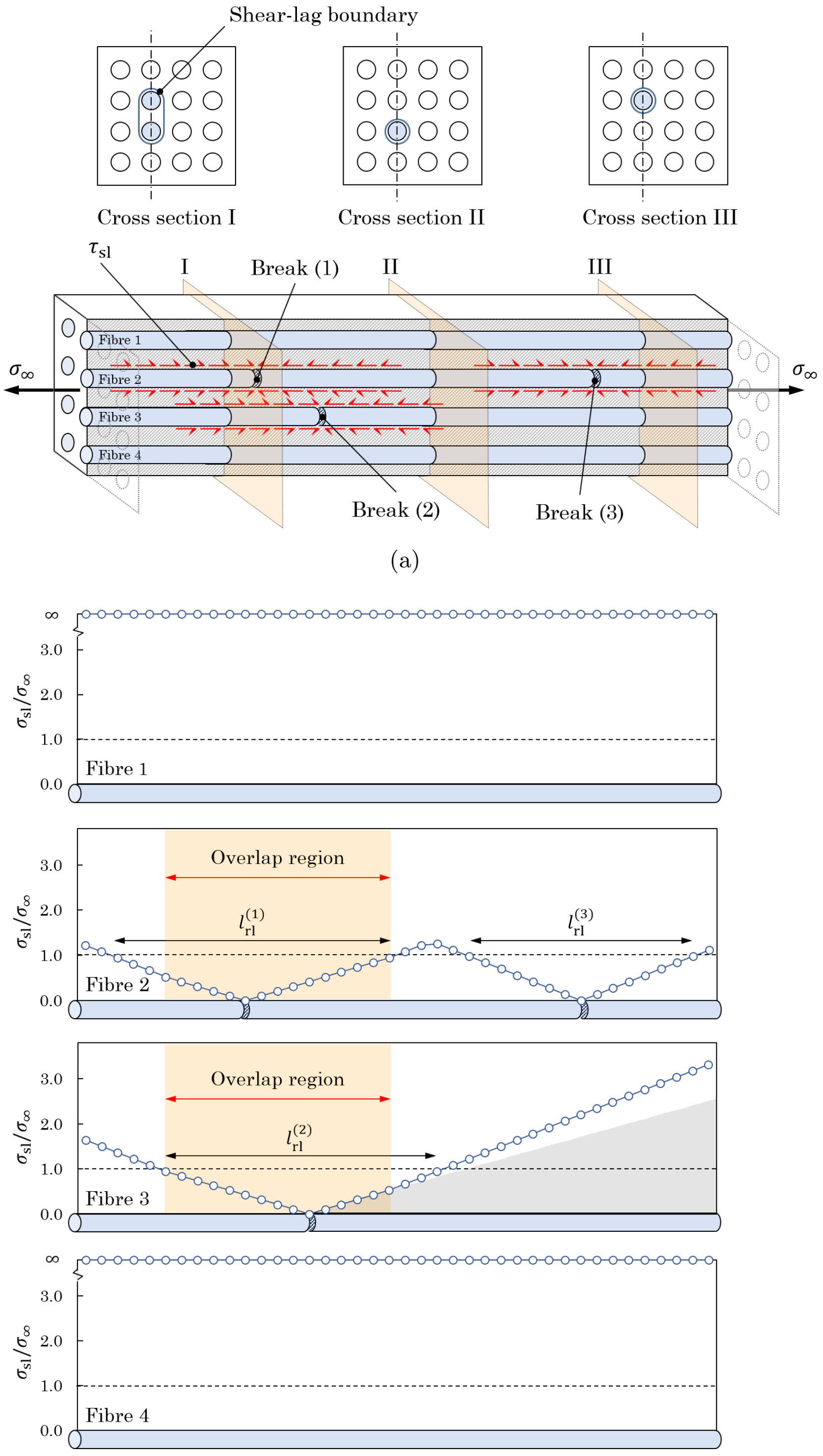

(a)

(b)

Figure 4: Shear-lag mechanism and shear-lag stress limit. (a) Shear-lag mechanism and different cases of interaction between three breaks in a 16-fibre bundle, depending on the position z: overlap region recovery lengths and cluster of broken fibres (cross section 1), non-overlap region (2), single broken fibre (3). (b) Shear-lag stress limit for fibres 1-4, with $n_{\mathrm{el}} = 40$. The shadowed triangle in the third chart is included to show the change in the slope in the overlap region due to the cluster.

but starting each iteration with the field σ^{ij} calculated at the previous step instead of σ_∞.

The stress field for fibres 1-4 of Fig. 4 is displayed in Fig. 5, using $\gamma = 2$. The appropriate value for this parameter was determined via a comparison with data of stress concentrations in bundles with clusters of broken fibres generated via FE simulations from St-Pierre et al. [22] (Fig. 6). The value of $\gamma = 2$ is shown in [22] to capture very well the stress concentration factor for clusters of various sizes and is used in all the simulations throughout the document.

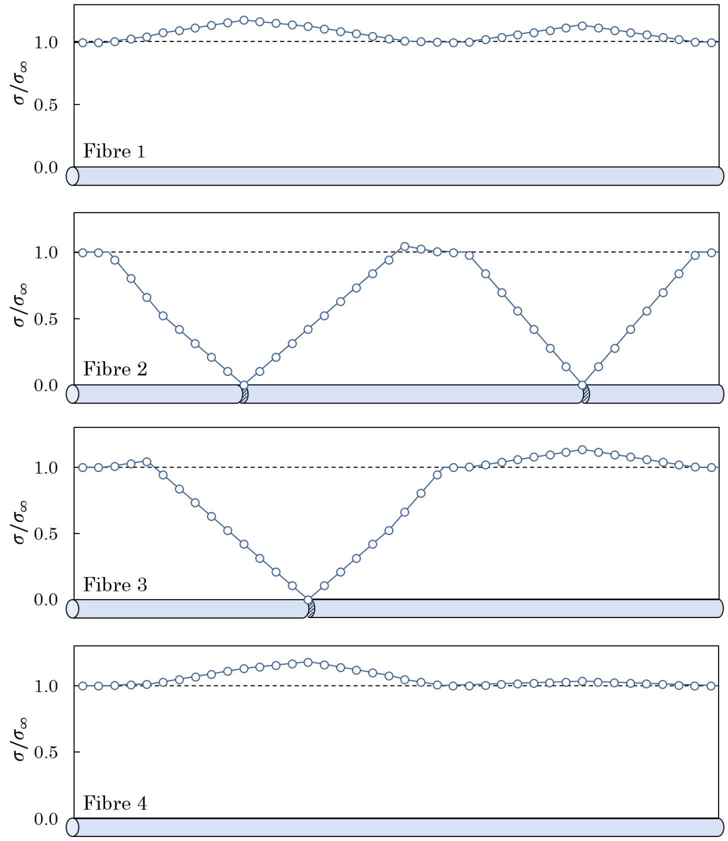

Figure 5: Stress redistribution for the fibres 1-4 of Fig. 4.

2.2.4. Failure simulation process

The bundle is loaded by imposing successive values of $\sigma_\infty(t^k)$ until final failure. As initial condition to start the simulation $\left(t^k = 0\right)$, the bundle is loaded to $\sigma_\infty(t^k = 0) \leftarrow \min(X^{ij})$ to break the weakest fibre element.

The stress dropped by the failed elements is redistributed over the intact elements following the procedure described in Sections 2.2.2 and 2.2.3, and the new stress state in the bundle is calculated

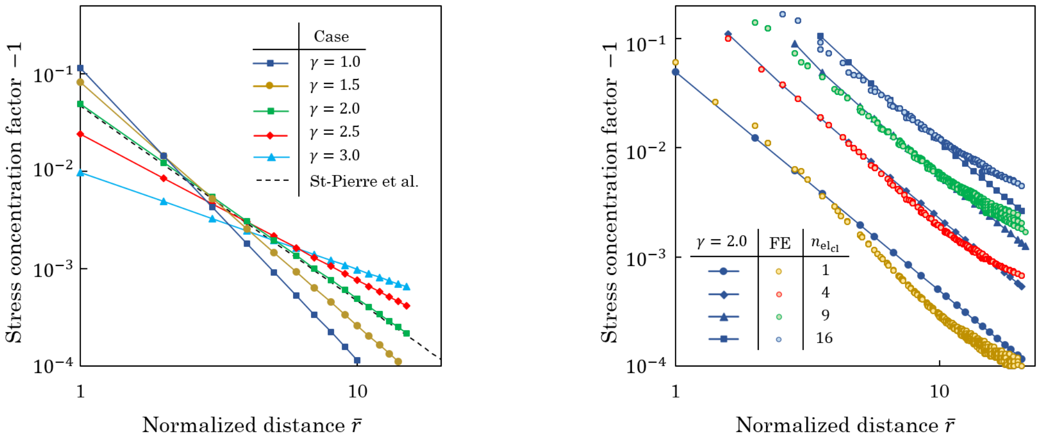

(a) (b)

Figure 6: Distribution of the stress concentration factor in the cross section of a bundle of $n_{\mathrm{f}} = 900$ fibres with a cluster of broken fibres in the centre. Geometry of the bundle and material properties are defined in Table 1 of St-Pierre et al. [22]. (a) Stress concentration factor as a function of the normalised distance $\bar{r}$ to an individual broken fibre, calculated by the current model for different values of the parameter γ, and the corresponding analytical solution from St-Pierre et al. with $\alpha = 2$ (see [22]). (b) Stress concentration factor as a function of the normalised distance $\bar{r}$ to the centre of a cluster of $n_{\mathrm{el_{cl}}}$ broken fibres calculated by the current model with $\gamma = 2$ and validated against FE results from [22].

while keeping the value of the asymptotic stress constant. At this point, a reserve factor $R^{ij}(t^k)$ is calculated for each fibre element in the bundle:

$$R^{ij}(t^k) = \frac{X^{ij}}{\sigma^{ij}(t^k)}. \tag{8}$$

Two different scenarios are possible depending on whether all elements are able to withstand the current stress level ($R^{ij}(t^k) > 1 \ \ \forall \ (ij)$), or whether some elements are experiencing a stress level over their assigned strength ($\exists \ (ij) : \ \ R^{ij}(t^k) \leq 1$). In the first scenario, the asymptotic stress is increased to break a new element in the bundle:

$$\sigma_\infty(t^{k+1}) \leftarrow R_{\min}(t^k) \cdot \sigma_\infty(t^k), \tag{9}$$

where $R_{\min}(t^k) = \min\{R^{ij}(t^k)\}$ is the minimum reserve factor of all the elements in the bundle. In the second scenario, one or more fibre elements are due to fail under the current stress state. Two different approaches have been considered:

(i) the first is a *single break approach*, where the stress level is updated according to Eq. (9) thus failing only the element with the lowest reserve factor. Fig. 7a shows the variation of $\sigma_\infty(t^k)$

during the damage simulation for a square bundle with 16 fibres using this approach. The blue bands indicate the steps with fibre elements failing under the stress concentration; in these cases, σ_∞ decreases from step t^k to step t^{k+1}.

(ii) The alternative is a *multiple breaks approach*, where all elements which have $R^{ij} \leq 1$ are failed in the same time step, while the asymptotic stress is maintained constant $\sigma_\infty(t^{k+1}) \leftarrow \sigma_\infty(t^k)$. The stress is redistributed again in the subsequent step of the simulation, potentially causing more breaks. The process is repeated until all elements in the bundle can withstand the current level of stress, then the asymptotic stress is increased again following Eq. (9); or the final failure of the bundle is reached (Fig. 7b). In this approach, σ_∞ never decreases.

In both cases, the simulation process ends when an entire cross section becomes saturated ($(ij) \in \mathbb{N}^j_{\mathrm{st}}\ \forall\ (ij) \in$ cross section j), thus the force equilibrium is not possible. For the single break approach, the simulation is also stopped if $\sigma_\infty(t^{k+1})$ decreases to 70% of the maximum asymptotic stress. The bundle strength is assumed to be $X_{\mathrm{b}} = \max\{\sigma_\infty(t^k)\}$.

No strong evidence was found to decide *a priori* which approach is the most suitable between (i) and (ii). On the one hand, the single break approach is appealing because it can account for the fact that, in reality, no two elements fail exactly at the same time, and each failed element changes the state of stress in the bundle. On the other hand, the multiple breaks approach is widely used for other statistical strength models in the literature [5, 14, 22–24, 26–29, 44–49], and allows for significantly faster simulations given that the stress state does not have to be re-computed for each failed element.

In order to compare both approaches, a model BA.4 was implemented, which shares the same algorithm as model BA.3 but implementing a single break approach; while models BA.1 to BA.3 use a multiple breaks approach. The differences they introduce in the simulations will be discussed in Section 3.1. To the knowledge of the authors, it is the first systematic comparison of single and multiple breaking approach in a fibre bundle model.

2.2.5. Monte Carlo stopping criterion

The selection of an appropriate number of Monte Carlo simulations is critical to ensure the accuracy of the model predictions. Most models in the literature use a fixed number of simulations for all

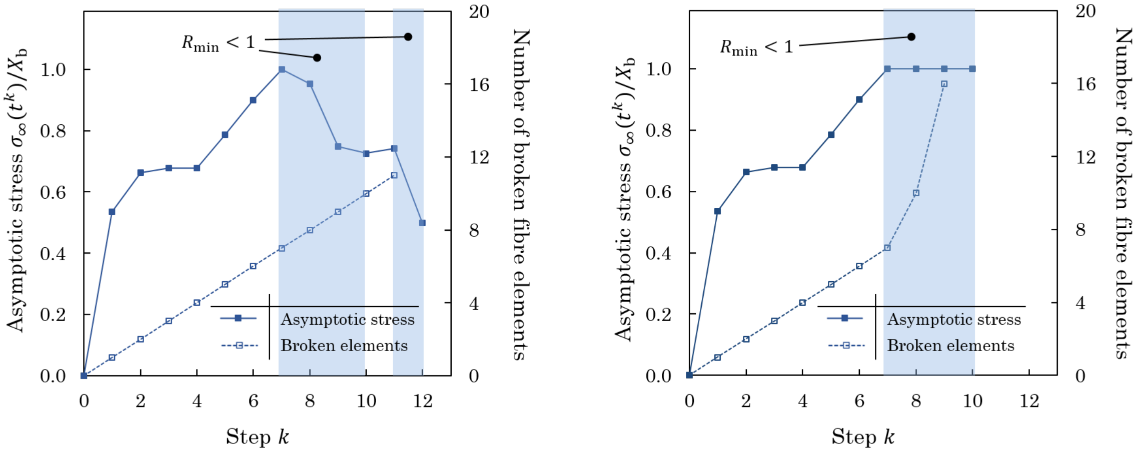

(a)

(b)

Figure 7: Damage simulation and evolution of $\sigma_\infty(t^k)$ in a 16-fibre bundle; geometrical and material properties are detailed in Table 2. (a) Single breaking approach; (b) Multiple breaking approach. The two approaches are coincident when $R_{\min} \geq 1$ but diverge when $R_{\min} < 1$ (these steps are highlighted with blue bands).

bundles sizes, despite the fact that both experiments and models show a decrease in the bundle strength variability when increasing the number of fibres in the bundle [29, 50, 51]. In this work, a bundle-size variable number of simulations was implemented as a way of increasing computational efficiency, while keeping the accuracy of the results constant.

Given a sample with N simulations, and following the Central Value Theorem, it is possible to calculate the confidence interval at 95% as

$$w_{\mathrm{CI}}^{95\%} = \left[\bar{X}_\mathrm{b} - t(N-1, 0.025) \cdot \frac{SD_\mathrm{b}}{\sqrt{N}}, \bar{X}_\mathrm{b} + t(N-1, 0.025) \cdot \frac{SD_\mathrm{b}}{\sqrt{N}}\right], \tag{10}$$

where $t(N-1, 0.025)$ is the value of the Student's-t distribution with $N-1$ degrees of freedom for a cumulative probability of 97.5%. The mean $\bar{X}_\mathrm{b}$ and standard deviation SD_b of the bundle strength from the sample are used as estimators of the equivalent normal distribution parameters.

Fig. 8 shows the flowchart of the implementation of this criterion in the model. The number of Monte Carlo simulations performed is the minimum that assures that the width of the confidence interval predicts the mean strength with a maximum accepted error $\pm e_{\bar{\mathrm{X}}}$. A value of $e_{\bar{\mathrm{X}}} = 1\%$ is used for all the simulations in the document (see Appendix C for more details on the choice of the maximum accepted error). Additionally, a minimum number of Monte Carlo simulations $N_{\min} = 12$ is set to ensure that the initial estimation of the mean and standard deviation are statistically meaningful.

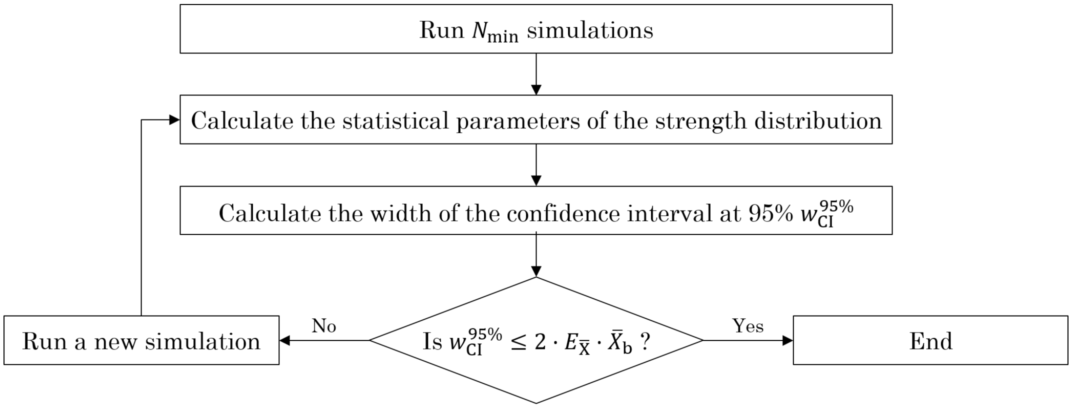

Figure 8: Flowchart of the Monte Carlo stopping criterion.

2.3. Dynamic effects model

In this section, the first model variant (hereafter referred to as model DE) is implemented to investigate the effects of dynamic stress concentrations on the bundle failure process and final strength.

The baseline model BA, as almost the totality of the FBMs in the literature, only considers the static equilibrium stress field when simulating damage. In reality, when a fibre fails, the stored elastic energy is released in form of a dynamic stress wave. This wave propagates throughout the intact fibres during a short time interval of duration $\Delta t_{\mathrm{dyn}}^{k}$ (hereafter designated as transient interval), causing a dynamic stress concentration, before it is dampened by the material and the stress field reverts to the static equilibrium one (Fig. 9).

When incorporating dynamic effects, the model definition and post-processing are the same used for the baseline model as described in Sections 2.2.1 and 2.2.5, whereas the failure simulation procedure is modified. The damage in the bundle can progress either through (i) fibre failure due to the dynamic stress concentration during the transient interval $\Delta t_{\mathrm{dyn}}^{k}$, or (ii) fibre failure due to an increase of the (quasi-static) asymptotic stress $\sigma_{\infty}(t^{k})$. Since the characteristic time for dampening the dynamic effects (transient interval) is much shorter that the time-scale required for varying the asymptotic stress, it is assumed that dynamic failure occurs under constant remote stress.

In the first time scale (*dynamic time scale*), associated with the damage created during the dynamic wave propagation, an upper bound for the effect of the dynamic stress field is obtained as described in Section 2.3.1 with the damage simulation approach described in Section 2.3.2. In the second time scale (*static time scale*), the dynamic effects have already disappeared and the stress field reverts to the static solution described in Section 2.2.3.

2.3.1. Dynamic stress field

Fig. 9 shows schematically the stress evolution in a fibre during the transient interval. In this model, we do not seek to simulate the stress evolution during the entire transient. Instead, we will estimate an upper-bound of the dynamic stress for each fibre, and use this for the implementation. In this way, comparing our static and dynamic predictions will reveal an upper-bound for the role of dynamic effects.

Considering that dynamic effects act by increasing the stress concentration on the intact fibres during the transient interval, it is assumed that the dynamic stress field σ_{dyn} can be computed using an expression similar to the static one in Eq. (7):

$$\sigma_{\text{dyn}}^{ij} = \begin{cases} \sigma_{\text{sl}}^{ij} & \text{if } \ ij \in \mathbb{N}_{\text{st}}^{j}; \\ \sigma_{\infty} + \lambda_{\text{dyn}} \cdot \sum\limits_{\mathbb{N}_{\text{st}}^{j}} \Delta\sigma^{(ij)_{\text{in}}(ij)_{\text{st}}} & \text{if } \ ij \in \mathbb{N}_{\text{in}}^{j}. \end{cases} \tag{11}$$

where λ_{dyn} is the dynamic magnification factor.

Dynamic stress concentrations have been reported to range between 160% and 200% of the corresponding static ones depending on the material properties and fibre packing [9, 18, 36–39]. The theoretical maximum dynamic magnification factor for a spring-mass system without damping subject to a step load is $\lambda_{\text{dyn}} = 2$. We will use this value for all fibre elements in this work, so as to obtain an upper-bound for the role of dynamic effects.

2.3.2. Damage simulation process

In model DE, the simulation is also initiated by making $\sigma_{\infty}(t^k = 0) \leftarrow \min\left(X^{ij}\right)$. The static stress field is computed using the same procedure as described in the baseline model; then, the dynamic stress field is calculated with Eq. (11).

If the dynamic stress concentration causes some elements in the bundle to experience a stress over their assigned strength ($\exists \ (ij) : \ \sigma_{\text{dyn}}^{ij} \geq X^{ij}$), the first fibre element in the wave path (the closest element to the previous point of failure) is the first one to fail, and it releases another dynamic wave

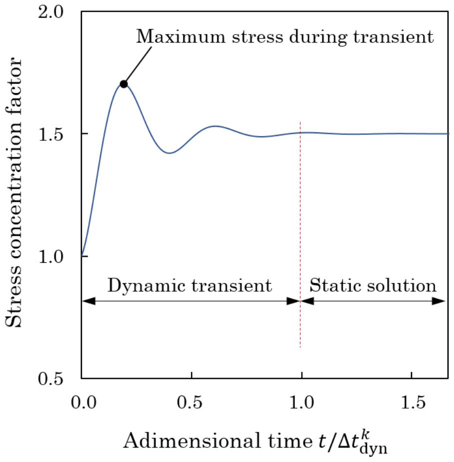

Figure 9: Schematic representation of the stress evolution during a dynamic transient.

which, in turn, can cause more element failures.

Since each fibre failure causes a variation of the dynamic stress levels, a single break approach is adopted and the dynamic stress field is re-calculated after each step. This process happens in the dynamic time scale, thus the asymptotic stress remains constant:

$$\sigma_\infty(t^{k+1}) \leftarrow \sigma_\infty(t^k). \tag{12}$$

When the dynamic stress concentration does not cause any new fibre element failure ($\sigma^{ij}_{\mathrm{dyn}} < X^{ij} \ \forall \ i,j$), the algorithm reverts to the static time scale, the stress state reverts to the static one and the reserve factor is calculated following Eq. (8). The simulation continues raising the asymptotic stress to break a new element:

$$\sigma_\infty(t^{k+1}) \leftarrow R_{\min}(t^k) \cdot \sigma_\infty(t^k). \tag{13}$$

2.4. Fracture mechanics model

During the failure process of the bundle, clusters of broken fibres may form due to initial fibre failures driven by strength-of-materials (stress overload), and may start acting as cracks in the material. If the energy release rate associated with these clusters/cracks is higher than the corresponding fracture toughness, they may trigger catastrophic failure. In this section, we propose a model that accounts for fracture mechanics driven failure from clusters of broken fibres, and will hereafter refer to it as model FM.

The structure of model FM is similar to that one of the baseline model BA: the calculation of the shear-lag stress limit, the stress redistribution and the damage simulation process are carried out in the same fashion, accordingly to Sections 2.2.2, 2.2.3 and 2.2.4 respectively. However, the size of each equivalent crack is monitored during the failure simulation, introducing an additional step at each iteration. Hence, if at any step of the simulation t^k a cluster of broken fibres reaches the critical cluster size for the applied remote load (which is determined using the fracture mechanics criterion described in Section 2.4.1), it is assumed to cause catastrophic failure of the bundle and $\sigma_\infty(t^k)$ is taken as the bundle strength (Section 2.4.1). If no cluster ever reaches critical conditions, the simulation follows the same procedure as in the baseline model.

2.4.1. Critical cluster size

When the recovery lengths associated with two or more failed elements belonging to neighbouring fibres overlap, all the fibre elements inside the overlapping regions are considered to be part of the same cluster (Section 2.2.2). Thus, it is possible to define n_{cl} sets $\mathbb{N}^s_{\mathrm{cl}}$ of fibre elements in the bundle (with $s = 1, ..., n_{\mathrm{cl}}$) which correspond to each cluster.

Additionally, in each bundle cross section j, it is possible to define different sets $\mathbb{N}^{sj}_{\mathrm{cl}}$ of neighbouring fibre elements associated with the cluster s in section j. Each set $\mathbb{N}^{sj}_{\mathrm{cl}}$ contains $n^{sj}_{\mathrm{el_{cl}}}$ elements $(ij)^s_{\mathrm{cl}}$ and can be idealised as an equivalent translaminar crack with equivalent characteristic crack size (see Fig. 10):

$$a^{sj}_{\mathrm{eq}} = \sqrt{\frac{4 \cdot n^{sj}_{\mathrm{el_{cl}}} \cdot A_{\mathrm{f}}}{\pi \cdot V_{\mathrm{f}}}}. \tag{14}$$

As shown in Fig. 10, the equivalent crack is formed by failed fibre elements in neighbouring fibres which are included in the respective recovery lengths, but not necessary laying on the same bundle cross section. When the equivalent crack reaches critical conditions, the matrix interface between to neighbouring failed elements has already passed its yielding point and is considered to be failed. However, stress transfer between neighbouring fibres inside the cluster is still possible via friction stress. The average pull-out stress $\sigma^{sj}_{\mathrm{po}}$ due to the friction between the fibre pull-outs is

$$\sigma^{sj}_{\mathrm{po}} = \frac{\sum\limits_{\mathbb{N}^{sj}_{\mathrm{cl}}} \tau_{\mathrm{fr}} \cdot C_{\mathrm{f}} \cdot |z^{(ij)^s_{\mathrm{cl}}} - z^{(ij)_{\mathrm{fa}}}|}{n^{sj}_{\mathrm{el_{cl}}} \cdot A_{\mathrm{f}}}, \tag{15}$$

where τ_{fr} is the friction stress acting on the lateral surface of each fibre pull-out (Fig. 10b) and $|z^{(ij)^s_{\mathrm{cl}}} - z^{(ij)_{\mathrm{fa}}}|$ is the pull-out length (i.e. distance between the element belonging to the equivalent crack in cross section j and the closest failed element along the same fibre i belonging to the cluster). The pull-out stress decreases the energy available for crack propagation, and reflects the fact that clusters of broken fibres which are almost co-planar are more likely to become critical than clusters which are more dispersed.

Therefore, an equivalent stress $\sigma^{sj}_{\mathrm{eq}}$ which drives the propagation of the equivalent crack can be calculated considering that (i) the fundamental driving force for crack propagation is the asymptotic stress σ_∞, (ii) there is a pull-out stress components due to the friction between fibre pull-outs inside the equivalent crack thus stress can still be transferred between the two faces of the equivalent crack, and (iii) the axial load is not carried by the entire cross section but only by the fibres:

$$\sigma^{sj}_{\mathrm{eq}} = V_{\mathrm{f}} \cdot \left(\sigma_\infty - \sigma^{sj}_{\mathrm{po}}\right). \tag{16}$$

In order to determine the conditions for critical propagation of this equivalent crack, the analytical solution developed in [58] for the energy release rate of a flat penny-shaped crack in a fibre composite is used (Appendix B). The critical cluster size for the equivalent crack will be inversely proportional to the square of the equivalent stress σ_{eq}:

$$a^{sj}_{\mathrm{cr}} = \frac{\lambda_{\mathrm{fm}}}{(\sigma^{sj}_{\mathrm{eq}})^2}, \tag{17}$$

where λ_{fm} is a proportionality factor (with units $[\mathrm{m} \cdot \mathrm{MPa}^2]$) which allows to distinguish between the clusters becoming critical due to translaminar cluster growth (Eq. A9 in Appendix B)

$$\lambda^{\mathrm{T}}_{\mathrm{fm}} = \frac{2 \cdot \sqrt{E_1 \cdot \mu_{12}} \cdot G_{\mathrm{Tc}}}{S_{\mathrm{T}}}, \tag{18}$$

or due to longitudinal splitting (Eq. A10 in Appendix B)

$$\lambda^{\mathrm{L}}_{\mathrm{fm}} = \frac{4 \cdot E_1 \cdot G_{\mathrm{Lc}}}{S_{\mathrm{L}}}, \tag{19}$$

where a is the crack length, E_1 is the composite tensile modulus, μ_{12} is the composite in plane shear modulus and G_{Tc} and G_{Lc} are the critical energy release rates for translaminar and longitudinal crack propagation respectively. S_{T} and S_{L} are the finite width corrections factors (the methods for calculating them are detailed in [58]) and they both tend to π for large bundles. Therefore, we are considering $S_{\mathrm{T}} = S_{\mathrm{L}} = \pi$ for the scope of this model.

Note that in both cases (splitting and cluster growth), Eq. (17) predicts that the critical cluster size should be inversely proportional to $(\sigma_{\mathrm{eq}}^{sj})^2$, but with a different proportionality constant. Because of this, of the idealisation involved with the analogy with the penny-shaped crack problem, and of uncertainty in the measurement of the property in Eq. (18) and Eq. (19), in this work we will obtain predictions for a wide range of values of λ_{fm} and then relate this to values of the critical energy release rate for translaminar and longitudinal crack propagation (G_{Tc} and G_{Lc}) that can be obtained using Eq. (A9) and Eq. (A10) in Appendix B.

The fracture toughness failure criterion described above is implemented in the bundle failure simulation as follows. At each step of the simulation, the equivalent cracks for each cluster of broken fibres are identified at each bundle cross section and the cluster criticality index is calculated as

$$I_{\mathrm{cl}}^{sj} = \frac{a_{\mathrm{eq}}^{sj}}{a_{\mathrm{cr}}^{sj}}. \tag{20}$$

If during the failure simulation $I_{\mathrm{cl}}^{sj} \geq 1$ for any equivalent crack, the bundle is considered failed and the remote stress at that step is taken as the final bundle strength ($X_{\mathrm{b}} = \sigma_{\infty}(t^k)$).

2.5. Models flowcharts

In order to analyse all the features described above, six different models were created (see Table 1). Four correspond to different versions of model BA, implementing different strategies for the damage simulation or the calculation of the shear-lag stress limit. Models DE and FM are the model variants implementing dynamic effects and fracture mechanics, respectively.

The flowcharts corresponding to one Monte Carlo simulation of each model are presented in Figs. 11-13, with the most important differences highlighted in yellow. Models BA and DE consider strength of materials as the only failure theory, so the end of the simulation is subject to fibre stress overload. Model FM introduces the fracture mechanics driven failure, so simulations can also end when any cluster becomes critical.

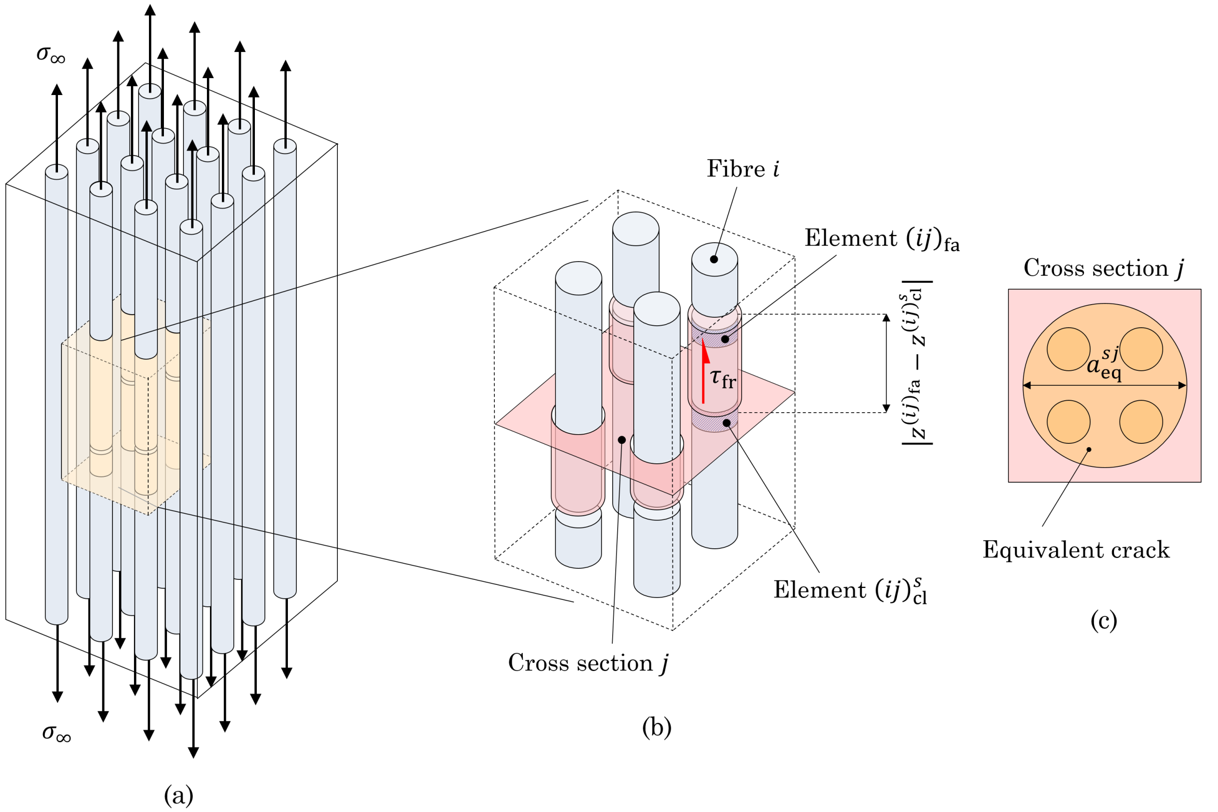

Figure 10: Fracture mechanics in the model. (a) Composite bundle loaded in tension with a cluster of broken fibres (highlighted in orange). (b) Detail of the pull-out phenomenon: to create the crack on the equivalent cross section j, apart from breaking the fibres it is necessary to pull a certain fibre length (red cylinders) out of the matrix, acting against τ_{fr}. (c) Equivalent crack and definition of the equivalent crack size. For a better understanding of the nomenclature and phenomena involved see Appendix B.

Additionally, all the models implement the Monte Carlo stopping criterion described in Section 2.2.5 to improve their computational efficiency.

Table 1: Models developed and key algorithm differences between them.

Ref.	Model family	Failure simulation	Shear-lag stress limit
BA.1	Baseline	Multiple breaks	Initial solution
BA.2	Baseline	Multiple breaks	Simplified
BA.3	Baseline	Multiple breaks	Exact
BA.4	Baseline	Single break	Exact
DE	Dynamic effects	Single break	Simplified
FM	Fracture mechanics	Multiple breaks	Simplified

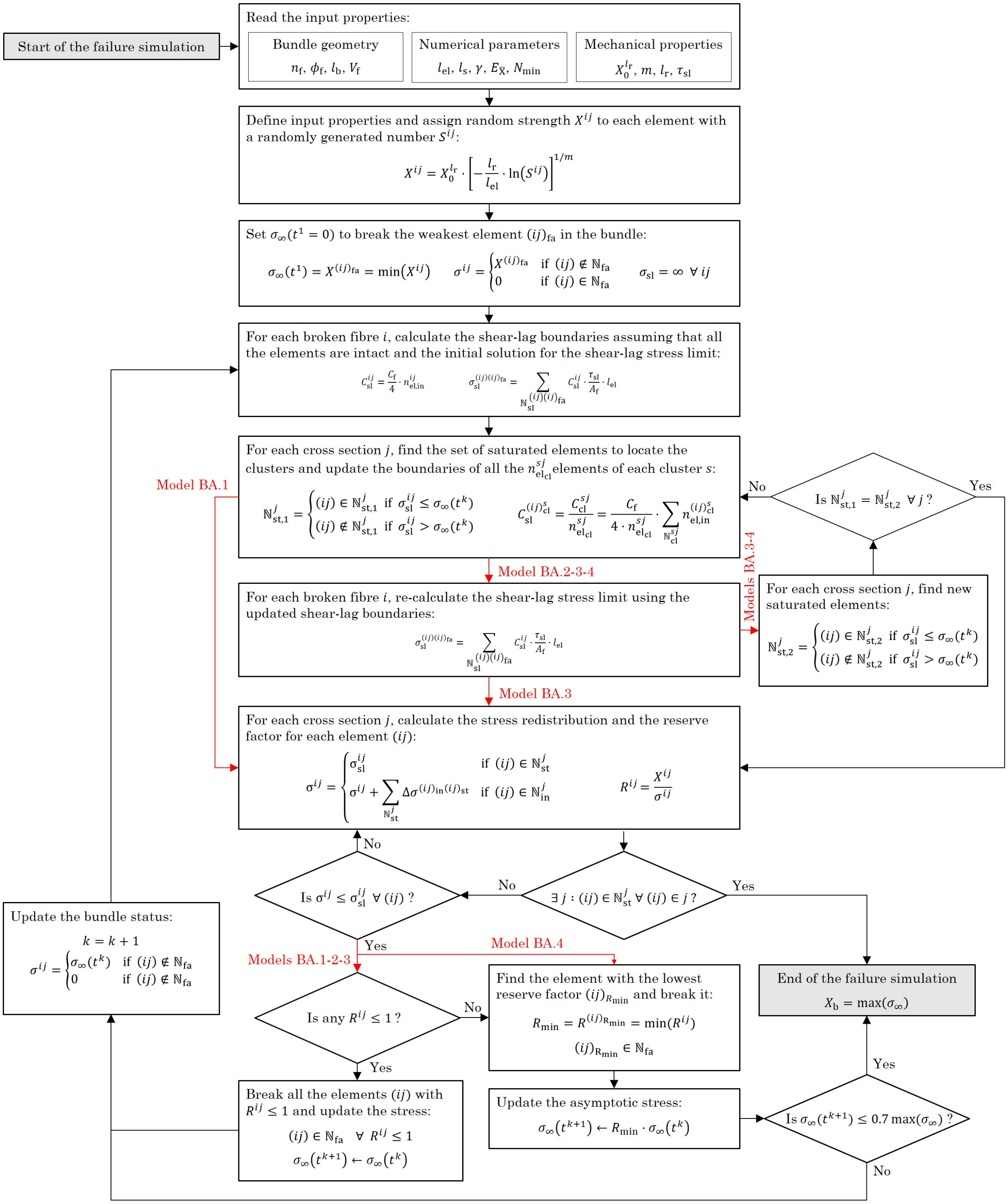

Read the input properties:

Define input properties and assign random strength X^{ij} to each element with a randomly generated number S^{ij}:

$$X^{ij} = X_0^{l_{\mathrm{r}}} \cdot \left[-\frac{l_{\mathrm{r}}}{l_{\mathrm{el}}} \cdot \ln\left(S^{ij}\right)\right]^{1/m}$$

Set $\sigma_\infty(t^1 = 0)$ to break the weakest element $(ij)_{\mathrm{fa}}$ in the bundle:

$$\sigma_\infty(t^1) = X^{(ij)_{\mathrm{fa}}} = \min\left(X^{ij}\right) \qquad \sigma^{ij} = \begin{cases} X^{(ij)_{\mathrm{fa}}} & \text{if } (ij) \notin \mathbb{N}_{\mathrm{fa}} \\ 0 & \text{if } (ij) \in \mathbb{N}_{\mathrm{fa}} \end{cases} \qquad \sigma_{\mathrm{sl}} = \infty\ \forall\, ij$$

For each broken fibre i, calculate the shear-lag boundaries assuming that all the elements are intact and the initial solution for the shear-lag stress limit:

$$C_{\mathrm{sl}}^{ij} = \frac{C_{\mathrm{f}}}{4} \cdot n_{\mathrm{el,in}}^{ij} \qquad \sigma_{\mathrm{sl}}^{(ij)(ij)_{\mathrm{fa}}} = \sum_{\mathbb{N}_{\mathrm{sl}}^{(ij)(ij)_{\mathrm{fa}}}} C_{\mathrm{sl}}^{ij} \cdot \frac{\tau_{\mathrm{sl}}}{A_{\mathrm{f}}} \cdot l_{\mathrm{el}}$$

For each cross section j, find the set of saturated elements to locate the clusters and update the boundaries of all the $n_{\mathrm{el_{cl}}}^{sj}$ elements of each cluster s:

$$\mathbb{N}_{\mathrm{st},1}^{j} = \begin{cases} (ij) \in \mathbb{N}_{\mathrm{st},1}^{j} & \text{if } \sigma_{\mathrm{sl}}^{ij} \le \sigma_\infty(t^k) \\ (ij) \notin \mathbb{N}_{\mathrm{st},1}^{j} & \text{if } \sigma_{\mathrm{sl}}^{ij} > \sigma_\infty(t^k) \end{cases} \qquad C_{\mathrm{sl}}^{(ij)_{\mathrm{cl}}^{s}} = \frac{C_{\mathrm{cl}}^{sj}}{n_{\mathrm{el_{cl}}}^{sj}} = \frac{C_{\mathrm{f}}}{4 \cdot n_{\mathrm{el_{cl}}}^{sj}} \cdot \sum_{\mathbb{N}_{\mathrm{cl}}^{sj}} n_{\mathrm{el,in}}^{(ij)_{\mathrm{cl}}^{s}}$$

For each broken fibre i, re-calculate the shear-lag stress limit using the updated shear-lag boundaries:

$$\sigma_{\mathrm{sl}}^{(ij)(ij)_{\mathrm{fa}}} = \sum_{\mathbb{N}_{\mathrm{sl}}^{(ij)(ij)_{\mathrm{fa}}}} C_{\mathrm{sl}}^{ij} \cdot \frac{\tau_{\mathrm{sl}}}{A_{\mathrm{f}}} \cdot l_{\mathrm{el}}$$

For each cross section j, find new saturated elements:

$$\mathbb{N}_{\mathrm{st},2}^{j} = \begin{cases} (ij) \in \mathbb{N}_{\mathrm{st},2}^{j} & \text{if } \sigma_{\mathrm{sl}}^{ij} \le \sigma_\infty(t^k) \\ (ij) \notin \mathbb{N}_{\mathrm{st},2}^{j} & \text{if } \sigma_{\mathrm{sl}}^{ij} > \sigma_\infty(t^k) \end{cases}$$

For each cross section j, calculate the stress redistribution and the reserve factor for each element (ij):

$$\sigma^{ij} = \begin{cases} \sigma_{\mathrm{sl}}^{ij} & \text{if } (ij) \in \mathbb{N}_{\mathrm{st}}^{j} \\ \sigma^{ij} + \sum_{\mathbb{N}_{\mathrm{st}}^{j}} \Delta\sigma^{(ij)_{\mathrm{in}}(ij)_{\mathrm{st}}} & \text{if } (ij) \in \mathbb{N}_{\mathrm{in}}^{j} \end{cases} \qquad R^{ij} = \frac{X^{ij}}{\sigma^{ij}}$$

Update the bundle status:

$$k = k + 1$$

$$\sigma^{ij} = \begin{cases} \sigma_\infty(t^k) & \text{if } (ij) \notin \mathbb{N}_{\mathrm{fa}} \\ 0 & \text{if } (ij) \notin \mathbb{N}_{\mathrm{fa}} \end{cases}$$

Find the element with the lowest reserve factor $(ij)_{R_{\min}}$ and break it:

$$R_{\min} = R^{(ij)_{\mathrm{R_{min}}}} = \min(R^{ij})$$

$$(ij)_{\mathrm{R_{min}}} \in \mathbb{N}_{\mathrm{fa}}$$

Break all the elements (ij) with $R^{ij} \le 1$ and update the stress:

$$(ij) \in \mathbb{N}_{\mathrm{fa}} \quad \forall\ R^{ij} \le 1$$

$$\sigma_\infty\left(t^{k+1}\right) \leftarrow \sigma_\infty\left(t^k\right)$$

Update the asymptotic stress:

$$\sigma_\infty\left(t^{k+1}\right) \leftarrow R_{\min} \cdot \sigma_\infty\left(t^k\right)$$

Figure 11: Flowchart of the model BA and its versions.

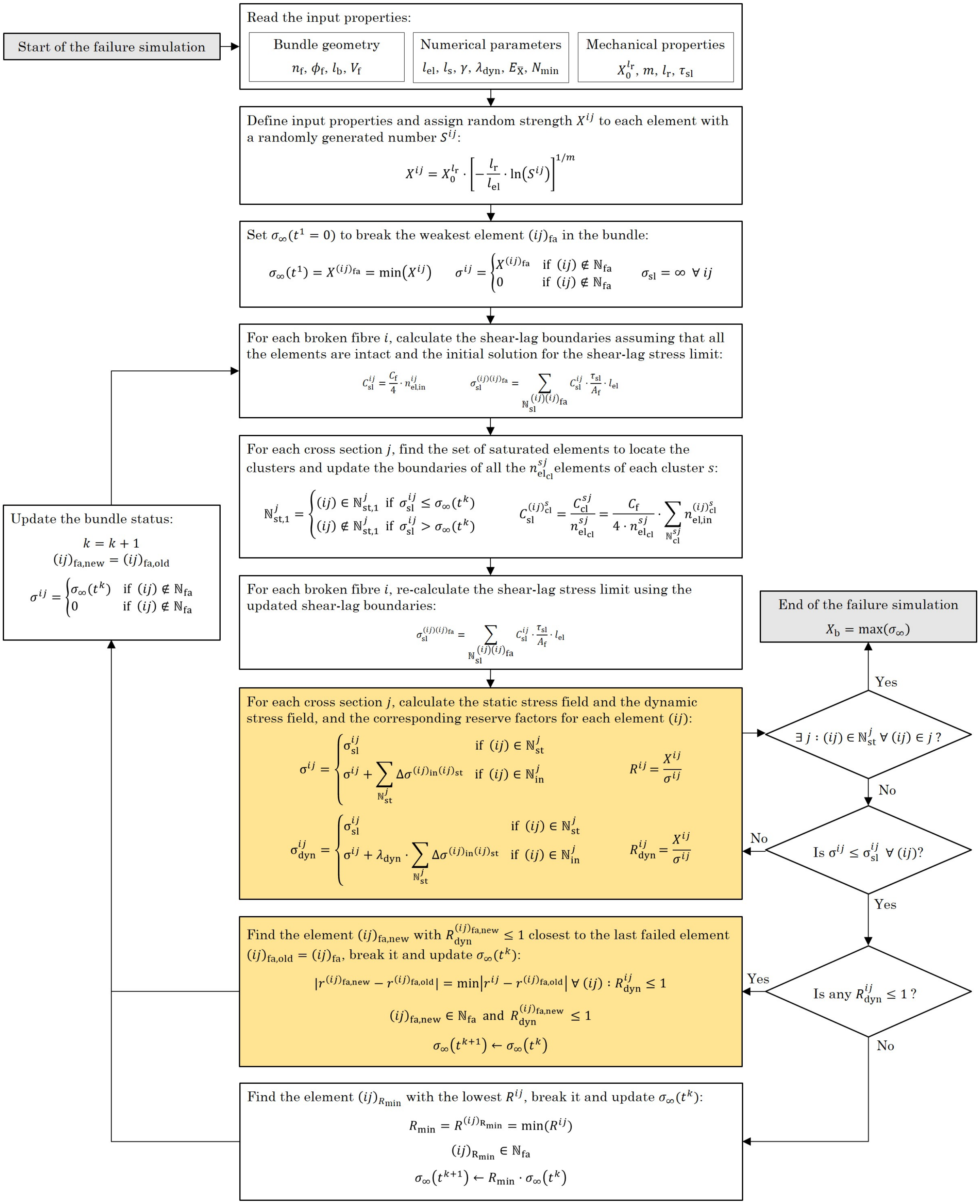

Figure 12: Flowchart of the model DE.

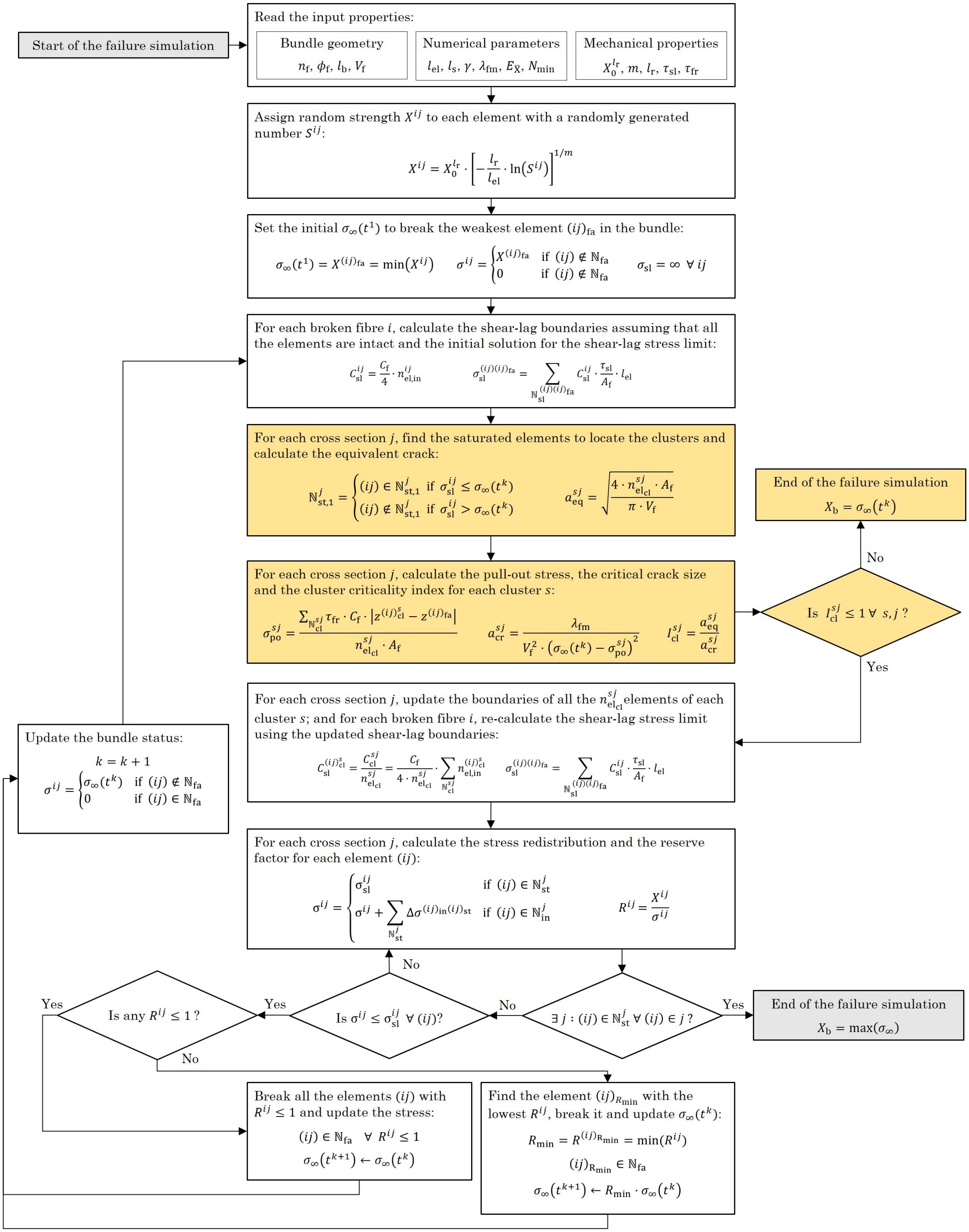

Figure 13: Flowchart of the model FM.

3. Results and discussion

This section compares the results provided by all the model variants described in Section 2 and validates the predicted strength distributions with respect to other modelling approaches from the literature and experimental data. Prior to the comparison, a numerical convergence study was carried out to select the appropriate numerical parameters, as discussed in Appendix C.

When presenting results for long bundles, a model with a representative simulation length l_s is firstly simulated and then the results are scaled to the desired bundle length l_b using the Weakest Link Theory (see details in Appendix D). This strategy is used to reduce the computational time of the simulations. No scaling is applied to the number of fibres in the bundle, which means that the actually desired number of fibres is simulated directly to obtain all the results.

3.1. Baseline model

3.1.1. Comparison of baseline model versions

Fig. 14 shows the comparison between the statistical bundle parameters predicted by the four versions of the baseline model. Bundle sizes up to 1600 fibres have been simulated and the results are presented for $l_\mathrm{b} = 10$ mm. The nominal input properties for the fibres and resin are listed in Table 2.

In general, all the model versions predict an increasing bundle strength with the number of fibres. Also, the variability decreases substantially with bundle size; thus the selection of a bundle-size variable number of Monte Carlo realisations is proven to be a very effective approach. The number of required simulations to keep the same confidence level decreases with the bundle size, allowing for significant savings in total computational time.

Fig. 14a compares the predicted bundle strength and variability for models BA.3 and BA.4. Both models perform the calculations with the exact shear-lag stress limit, but implementing a multiple breaks approach and a single break approach respectively. The two solutions are in almost exact agreement, suggesting that both approaches are equivalent with respect to the predicted bundle strength. However, Fig. 14b shows that the multiple breaks approach allows a slight improvement in terms of computational efficiency because the number of steps necessary for the simulations decreases as more fibre elements fail at each step.

Fig. 14c compares strength predictions with different estimations of the shear-lag stress limit: model BA.1 (initial solution for the shear-lag stress limit), model BA.2 (simplified shear-lag stress limit) and model BA.3 (exact shear-lag stress limit). Models BA.1 and BA.2 overestimate the mean strength and slightly reduce variability with respect to model BA.3. This result is expected because the non-exact solutions for the shear-lag stress limit may underestimate the recovery lengths, thus reducing the region of influence of the stress concentration. Although the difference between models BA.1 and BA.3 is significant (in general, larger than 10% for the mean strength), model BA.2 captures most of the effect of clusters on the recovery length, with a comparatively small error in the strength predictions.

Model BA.2, which uses the simplified shear-lag stress profile with a multiple breaks approach, allows a strong improvement of the computational cost (Fig. 14d), with a reduction of the average time per simulation by more than one order of magnitude in comparison with models BA.3 and BA.4. Given this consideration, and the small error in the prediction of the bundle strength, model BA.2 appears to be the most appropriate to conduct simulations on large bundle sizes, and will be used hereafter as the baseline model.

Table 2: Nominal input properties. Geometrical and mechanical properties are obtained from [5] and correspond to UD T800H/3631 composites (Toray).

Bundle geometry				Numerical parameters						Mechanical properties			
ϕ_f [µm]	l_b [mm]	Packing	V_f [-]	l_el [mm]	n_el [-]	l_s [mm]	γ [-]	$e_{\bar{\mathrm{X}}}$ [%]	N_min [-]	$X_0^{l_\mathrm{r}}$ [MPa]	m [-]	l_r [mm]	τ_sl [MPa]
5	10	Square	0.6	0.005	200	1	2.0	1.0	12	3570	3.8	50	52.4

3.1.2. Validation of modelling approach for large bundles

This section compares strength predictions from model BA.2 and from the 3D shear-lag model developed by Okabe et al. [26], which uses a shear and tension springs lattice to calculate the stress state in a fibre bundle with broken fibres. The 3D shear-lag model considers arrays of parallel fibres, each subdivided in smaller fibre elements, and uses a Weibull of Weibull (WOW) distribution to assign strength values to the individual fibre elements [5]; Monte Carlo simulations are used to generate statistical strength distributions for the bundle strength. In order to obtain a meaningful

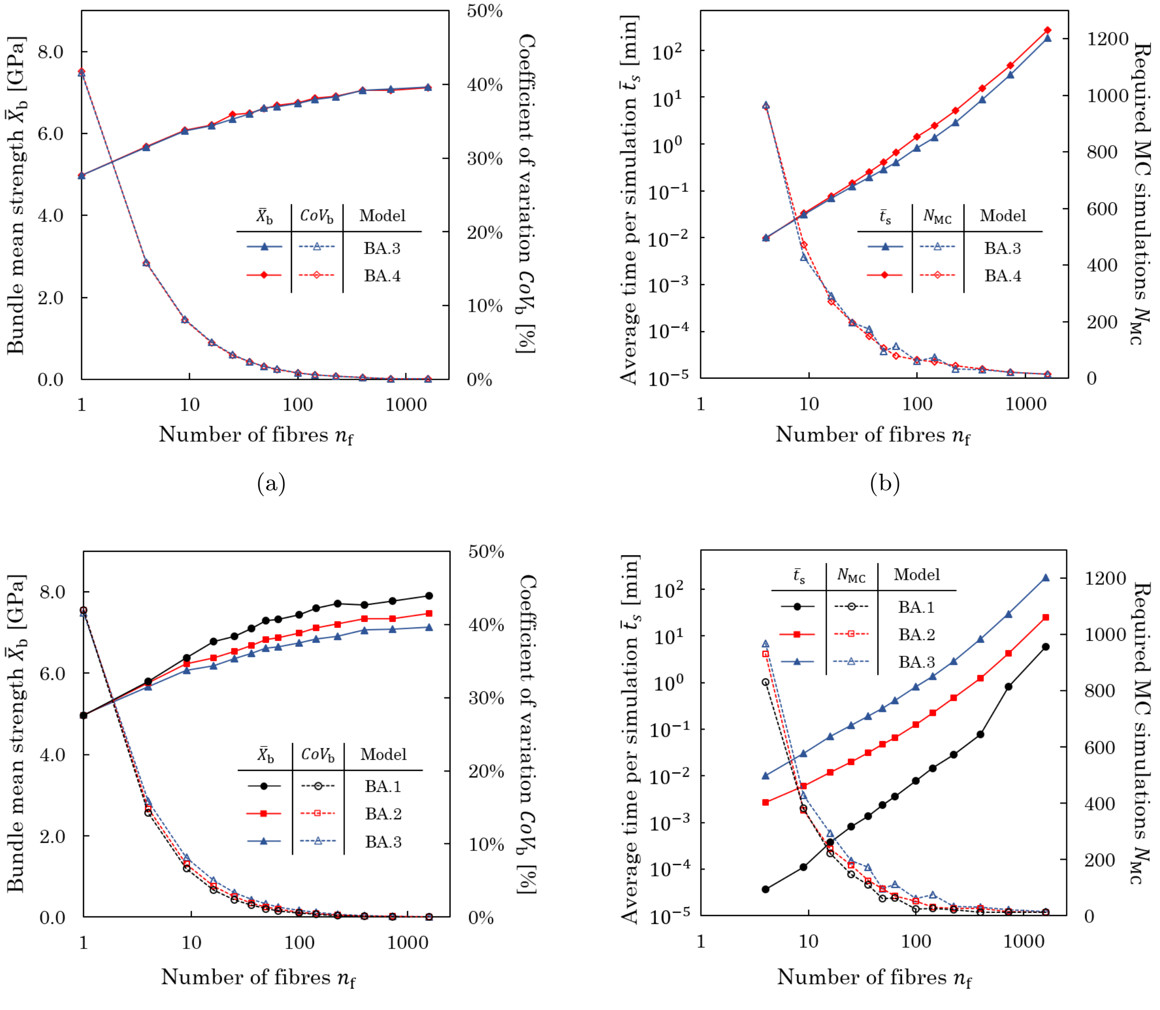

(a)

(b)

(c)

(d)

Figure 14: Simulation results for model BA variants. Results presented for a bundle length $l_b = 10$ mm. (a) Comparison of mean strength and coefficient of variation for models BA.3 (multiple breaks approach) and BA.4 (single break approach). (b) Comparison of computational cost for models BA.3 and BA.4. (c) Comparison of mean strength and coefficient of variation for models BA.1 (initial solution for the shear-lag stress limit), BA.2 (simplified shear-lag stress limit) and BA.3 (exact shear-lag stress limit) (d) Comparison of computational cost for models BA.1, BA.2 and BA.3.

comparison, we also implemented WOW in model BA.2 using the same formulation given in Okabe et al. [5] as described in Appendix E.

Fig. 15a-b compares the strength distributions predicted by model BA.2 and the 3D shear-lag model [26] for two different bundle sizes: $n_f = 324$ and $n_f = 1024$. The bundle length is $l_b = 0.8$ mm in both cases. The input parameters used for model BA.2 are given in Table 2, with the exception of the simulation length (which is $l_s = l_b = 0.8$ mm in this case) and the input properties for the WOW distribution, which are the same given in [5]: $\bar{X}_0^{l_r} = 3740$ MPa, $\rho_1 = 5.7$ and $\rho_2 = 5.4$ for

$l_\mathrm{r} = 50\,\mathrm{mm}$.

The results of model BA.2 exhibit an excellent correlation with 3D shear-lag model results; the differences in the average bundle strengths for bundles of 324 and 1024 fibres are -2.9% and a -2.1%, respectively. This good agreement validates the use of the analytical stress redistribution, and the failure algorithm used in this work. However, the analytical stress redistribution proposed is computationally inexpensive in comparison to solving numerically a large system of equations. This should allow the current modelling approach to be used for larger bundles, as will be shown in Section 3.5.

Finally, note that both models show an increase in strength with the number of fibres in the bundle, which is the opposite of the size effect expected (Fig. 15c). Therefore, both models, which are based exclusively on a strength of materials approach, do not appear to be able to predict the expected size effects, at least in this case.

3.2. Dynamic effects

This section compares the predictions given by model DE with model BA.2. The nominal input properties from Table 2 were used, and for model DE the simulations were carried out with $\lambda_\mathrm{dyn} = 2$. This case represents an upper-bound for the maximum intensity of the dynamic effects, and is meant to provide a theoretical lower-bound for the strength predictions. All results are presented for $l_\mathrm{b} = 10$ mm.

Fig. 16a shows the strength predictions given by models DE and BA.2. The difference in the predicted bundle strength is around 10%, but the increase in strength with the number of fibres remains. Also, variability is higher in model DE, thus increasing the number of Monte Carlo realisations and the computational time, as presented in Fig. 16b.

Considering dynamic stress concentrations does not vary the failure mechanism, so final failure is driven by strength of materials in both models. However, the average distance between consecutive breaks during the failure simulation is significantly smaller in model DE (Fig. 16d), suggesting that dynamic effects lead to clusters that are more co-planar. The formation of co-planar clusters during tensile tests is confirmed by computer tomography experiments [9] (see also Fig. 2), and is a feature that may eventually be related to dynamic effects. Therefore, the lower bundle strength predicted with including dynamic effects appears to be the result of the higher stress concentration and easier

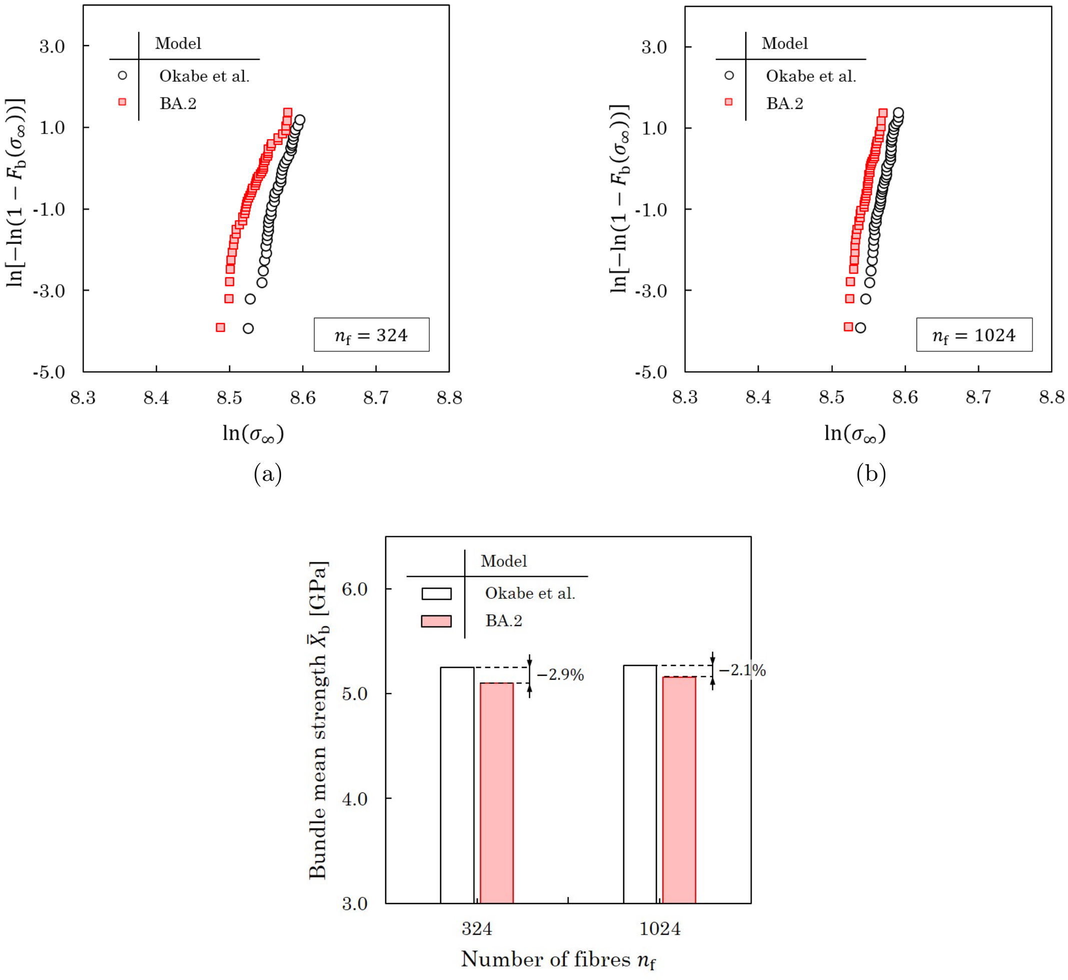

(a)

(b)

(c)

Figure 15: Simulation results for model BA.2 and the 3D shear-lag model from Okabe et al. [26]. Results are presented for $l_b = 0.8$ mm. (a) Predicted strength distributions for a bundle with $n_f = 324$. (b) Predicted strength distributions for a bundle with $n_f = 1024$. (c) Predicted mean strength and size effect for the bundles with $n_f = 324$ and $n_f = 1024$.

damage localisation around clusters of broken fibres introduced by the dynamic effects.

3.3. *Fracture mechanics*

In this section, we present the strength predictions for model FM, which features a fracture mechanics failure criterion. A parametric study was carried out analysing different values of λ_{fm} as a free parameter of the model so that its influence on the results may be investigated in detail. The nominal input properties (Table 2) were used, with $\tau_{fr} = 10$ MPa, $E_1 = 120$ GPa, $\mu_{12} = 4$ GPa and $\nu = 0.28$ to compute Eqs. (15), (18) and (19). All results are presented for $l_b = 10$ mm.

Fig. 17a compares the predicted strength and variability between model FM and model BA.2, for different values of λ_{fm}. It is observed that, when a fracture mechanics failure criterion is considered,

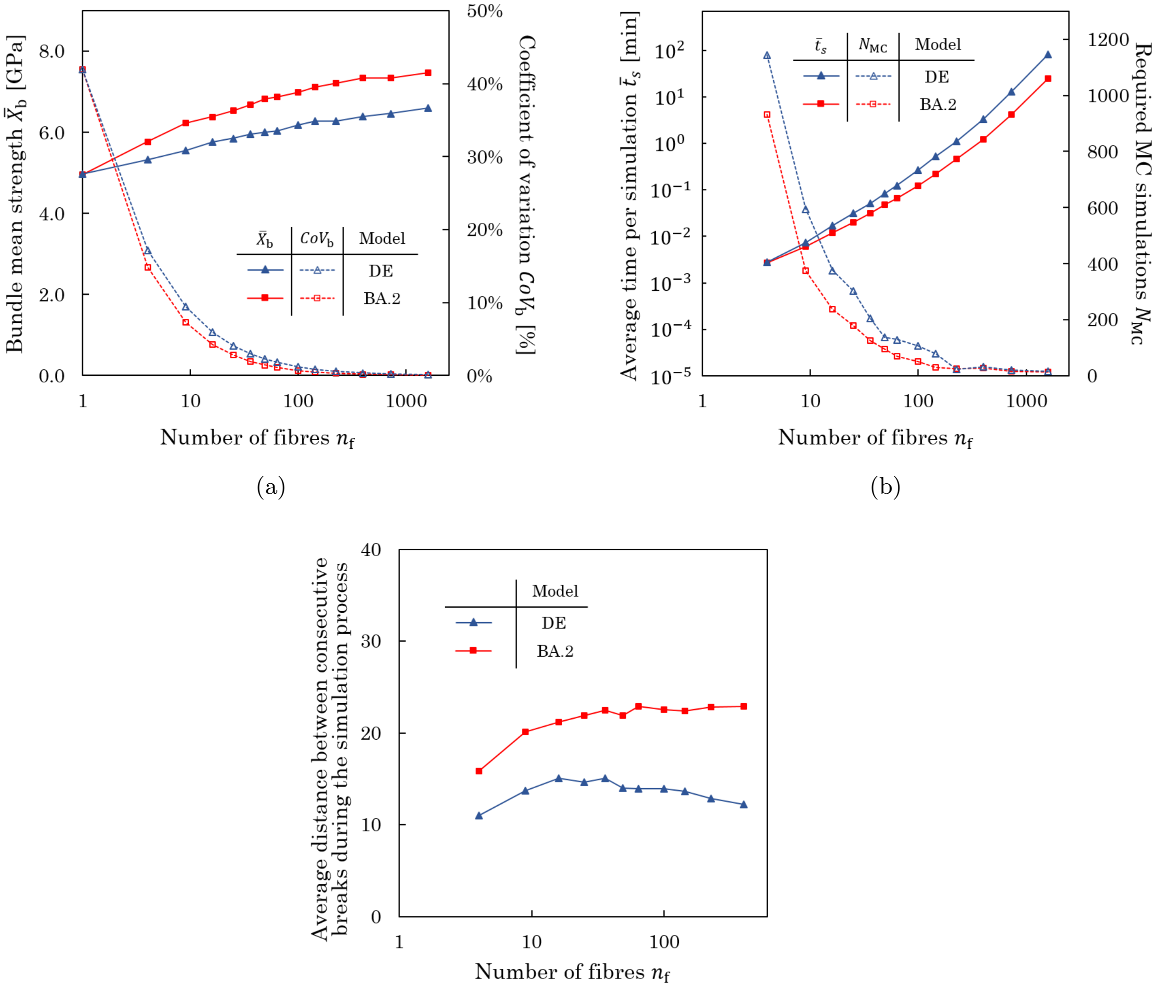

(a)

(b)

(c)

Figure 16: Simulation results for model DE. Results presented for a bundle length $l_b = 10$ mm. (a) Comparison of mean strength and coefficient of variation for models DE and BA.2. (b) Comparison of computational cost for models DE and BA.2. (c) Average distance (normalised with the fibre spacing s) between consecutive breaks during the simulation process for models DE and BA.2. In this case, the bundle length is $l_b = 1$ mm.

the predicted bundle strength decreases significantly. Furthermore, considering fracture mechanics can change the overall size effects for bundles with low values of λ_{fm}: strength presents a maximum for medium-size bundles (under 100 fibres) and then decreases with the bundle size. For higher values of λ_{fm}, the bundle strength tends to converge to model BA.2. Finally, the introduction of fracture mechanics does not cause significant change in the bundle variability, thus the number of Monte Carlo simulations is similar to that for model BA.2.

Fig. 17b shows the average critical cluster size as a function of the number of fibres for different values of λ_{fm} in model FM. These predictions are significantly smaller than n_f for large bundles.

Additionally, the critical cluster size appears to reach an horizontal asymptote. Although direct comparison with experimental results is not possible at this point, this result is in line with experimental evidence, which has not reported clusters greater than 14 fibres, even for large bundles [7, 9]. Other simulation models in the literature which do not consider fracture mechanics, also tend to severely overestimate the critical cluster size [7].

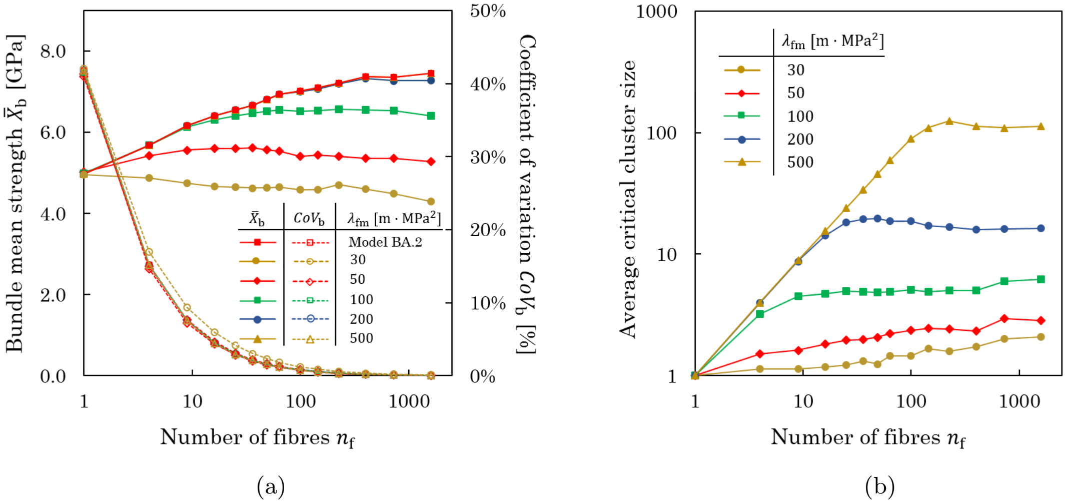

Figure 17: Simulation results for model FM. Results presented for a bundle length l_b = 10 mm.(a) Comparison of mean strength and coefficient of variation for models FM (with different values of λ_{fm}) and BA.2. (b) Average critical cluster sizes predicted by model FM (with different values of λ_{fm}).

It should be noted that, as the size of a cluster of broken fibres grows, it starts resembling a notch and the stress concentration at its edges tend to rise. As such, it is reasonable to expect that a strength of materials approach should be able to capture the destabilising effect of this severe stress concentration in a brittle material. However, by the addition of the fracture mechanics effects to the model, it is possible to capture the dissipative effect of friction during the pullout process as this is embedded in the fracture toughness values for the material. Such an effect would be more difficult to include in the basic strength of materials models. Eventually, enhanced approaches still based on strength of materials (e.g. using average stresses over a certain region [59–61]) could be able to capture this effect.

3.4. Validation against experimental results for micro-bundles

Fig. 18 shows a comparison between experimental strength data for composite micro-bundles and the strength distributions predicted by models BA.2 and DE. Model FM is not included in this comparison because the effect of fracture mechanics starts only to become significant for large bundles (Fig. 17a). When applicable, strength predictions for the same material system obtained via Monte Carlo simulation of a full FE bundle model from St-Pierre et al. [22] are included for comparison.

Fibre properties were taken from the experiments of Beyerlein and Phoenix [50] and Kazanci [51] and are listed in Table 3. Two different matrices were used in the experiments: matrix (I) is a low modulus epoxy, consisting of a blend of 50% DER 221 and 50% DER 732 with DEH 26 as curing agent; while matrix (II) is a high modulus epoxy, with a 100% of resin DER 331 with the same curing agent. The matrix yield stresses were obtained from Netravali et al. [62]; they are $\tau_{\text{sl}} = 3.96$ MPa and $\tau_{\text{sl}} = 41.67$ MPa for matrices (I) and (II), respectively.

Fig. 18a-d shows the comparison with four-fibre bundles and with two different lengths: 10 mm and 200 mm. All results were obtained using $l_{\text{s}} = 10$ mm in the model, which allowed direct comparison with experiments for bundles of $l_{\text{b}} = 10$ mm; while the comparison with bundles of $l_{\text{b}} = 200$ mm was performed scaling the modelling results using WLT (see Appendix D). For the low-strength matrix (I) the bundle strength distributions correlate very well and the predicted mean values do not deviate more than a 3.3% (Fig. 19).

For the higher-strength matrix (II), predictions with models BA.2 and DE appear to overestimate slightly the experimental strength, and are very close to the results of the FE simulations from St-Pierre et al. [22] which assumes shear lag with perfectly plastic behaviour of the matrix and no debonding with the fibres. It should be noted that Netravali et al. [62] have reported the occurrence of debonding at the fibre matrix interface during single fibre fragmentation tests with epoxy (I), while no debonding was observed for the flexible epoxy (II). Debonding at the fibre matrix interface results in a longer recovery length and this may lower the bundle strength (see Fig. 14c). This consideration may explain why both simulations tend to overestimate the experimental results.

Fig. 18e-f shows the comparison with experimental results for $l_{\text{b}} = 10$ mm micro-bundles with 7 fibres. The result were obtained by linear interpolation from square bundles of 4 and 9 fibres. In this case, predicted strength distributions for matrix (I) deviate slightly from the experimental data, while the agreement with matrix (II) is better.

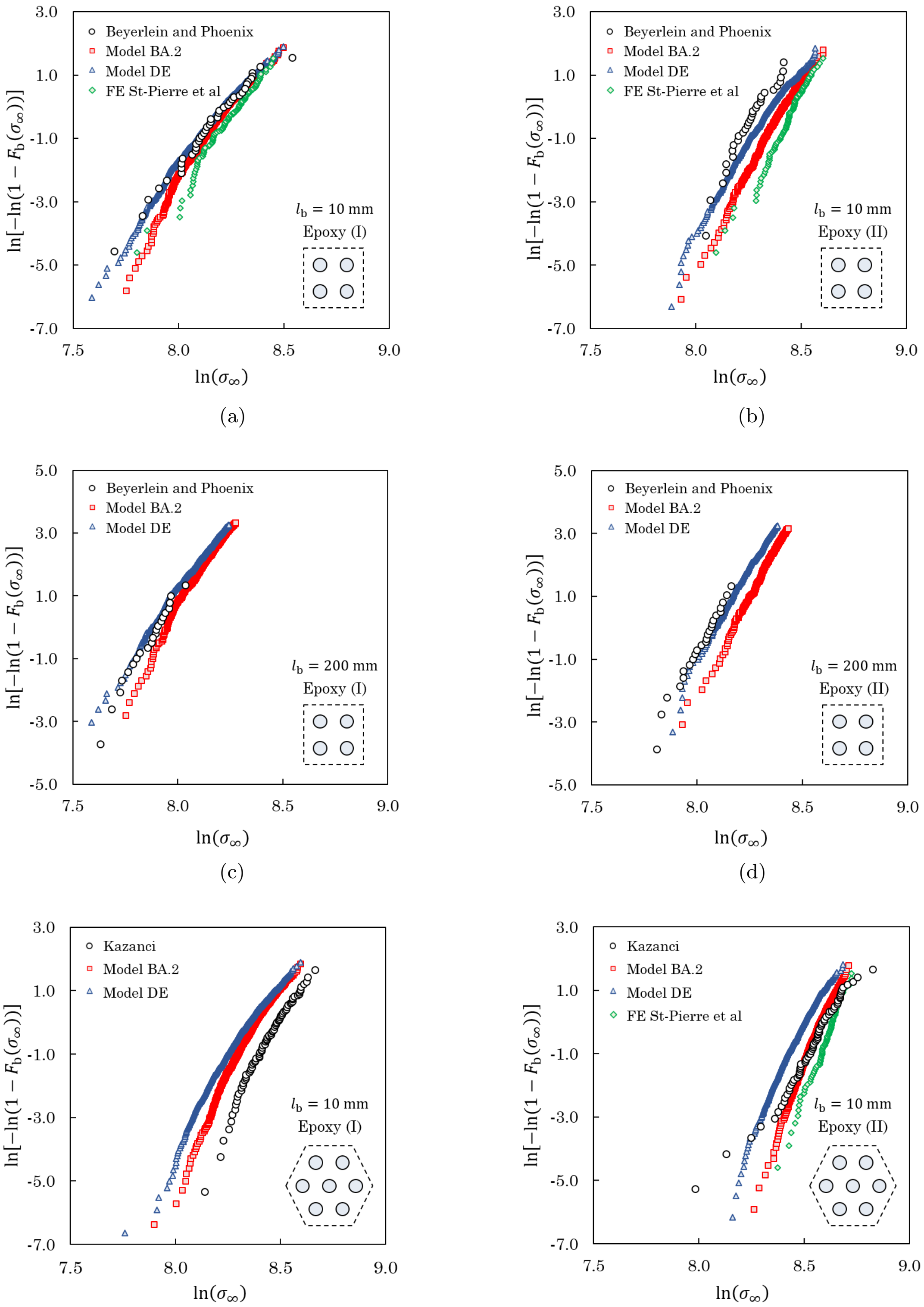

(a) (b) (c) (d) (e) (f)

Figure 18: Validation of models BA and DE with experimental data of micro-bundles and numerical modelling results from Okabe et al. and . (a) 4 fibres, epoxy (I), $l_\mathrm{b} = 10$ mm. (b) 4 fibres, epoxy (II), $l_\mathrm{b} = 10$ mm. (c) 4 fibres, epoxy (I), $l_\mathrm{b} = 200$ mm. (d) 4 fibres, epoxy (II), $l_\mathrm{b} = 200$ mm. (e) 7 fibres, epoxy (I), $l_\mathrm{b} = 10$ mm. (f) 7 fibres, epoxy (II), $l_\mathrm{b} = 10$ mm.

Table 3: Fibre properties and bundle geometry for the comparison with experimental data in micro-bundles. Obtained from [50, 51].

Reference	Fibre properties					Bundle geometry		
	Type	C_f [µm]	$X_0^{l_\mathrm{r}}$ [MPa]	m [-]	l_r [mm]	l_b [mm]	Packing	V_f [-]
Beyerlein and Phoenix (1997)	AS4	6.85	4493	4.8	10	10/200	Square	0.70
Kazanci (2004)	IM6	5.63	5283	5.4	10	10	Hexagonal	0.56

3.5. Comparison with macro-bundles

Fig. 20 compares experimental data for the bundle mean strength of composite bundles ranging from one thousand up to one million fibres obtained from Okabe and Takeda [5] with the predictions of the current models. Results were obtained with properties defined in Table 2 by simulating $l_\mathrm{s} = 1$ mm bundles and scaling the results to $l_\mathrm{b} = 10$ mm using WLT.

Fig. 20a shows the results predicted by models BA.2 and DE. Both models significantly overestimate the strength of large bundles. Furthermore, the size effect observed in the range of the experiments (decrease in strength with the number of fibres in the bundle) cannot be reproduced by any of the two models. These results suggest that the strength of large composite bundles, and in particular

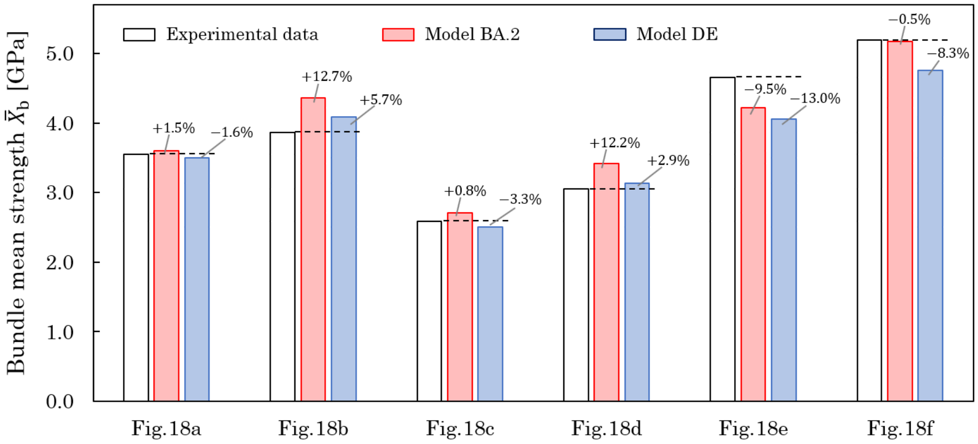

Figure 19: Statistical mean values predicted by models BA.2 and DE and compared with experimental data in Fig. 18. Deviation with respect to experiments is indicated in the chart.
The plotted values for each case are the following ones:
Experimental data [MPa]: 3553 (18a), 3868 (18b), 2587 (18c), 3049 (18d), 4661 (18e), 5193 (18f)
Model BA.2 [MPa]: 3605 (18a), 4359 (18b), 2710 (18c), 3422 (18d), 4220 (18e), 5169 (18f)
Model DE [MPa]: 3495 (18a), 4087 (18b), 2503 (18c), 3137 (18d), 4054 (18e), 4763 (18f)

the size effects, cannot be correctly predicted considering only strength of materials (even with dynamic stress concentrations) as a failure theory.

Fig. 20b compares the predicted bundle mean strength from Model FM with the experimental data. A parametric study was carried out by varying the value of λ_{fm} from 30 to 70 $\mathrm{m} \cdot \mathrm{MPa}^2$. The strength predictions from model FM are in the same range as the experimental results. Furthermore, the reduction in the predicted mean strength with the bundle size is compatible with the trend of the experimental data. Note that, although the predictions depend on λ_{fm}, the model predicts the correct size effect (reduction of strength with increase in the number of fibres) for all values of λ_{fm} considered. This suggest that failure in large composite bundles may be driven by fracture mechanics, and that size effects may not be reproducible via direct simulation only considering strength of materials.

The best fit in Fig. 20b occurs when $\lambda_{\mathrm{fm}} \sim 50$ $\mathrm{m} \cdot \mathrm{MPa}^2$. Substituting this value with the input properties in Eq. (18) and solving for the energy release rate, it is possible to obtain the corresponding value of critical energy release rate for translaminar crack propagation: $G_{\mathrm{Tc}} = 3.66$ $\mathrm{kJ/m}^2$. Carrying out the same procedure for Eq. (19) leads to the value of critical energy release for longitudinal crack propagation: $G_{\mathrm{Lc}} = 0.33$ $\mathrm{kJ/m}^2$. Both values of critical energy release rate are compatible with the respective properties of common fibre matrix systems [63–66] (although on the low end of the range), thus validating the hypothesis that final failure of a composite bundle can indeed be triggered by unstable propagation of critical clusters of broken fibres. However, from the present data it is not possible to determine weather the dominant crack propagation mode is longitudinal or translaminar.

4. Conclusions

A family of semi-analytical fibre bundle models was developed to efficiently simulate the longitudinal tensile failure of large composite bundles. A field superposition method was used by all the models to calculate the stress concentration around clusters of broken fibres, and has been validated against analytical and FE results from the literature. To the knowledge of the authors, this is the first time that a field superposition method was shown to be able to capture the effect of clusters of broken fibres on the stress recovery length. Additionally, a method with a bundle-size dependent variable number of Monte Carlo simulations was implemented to improve the computational efficiency, hence

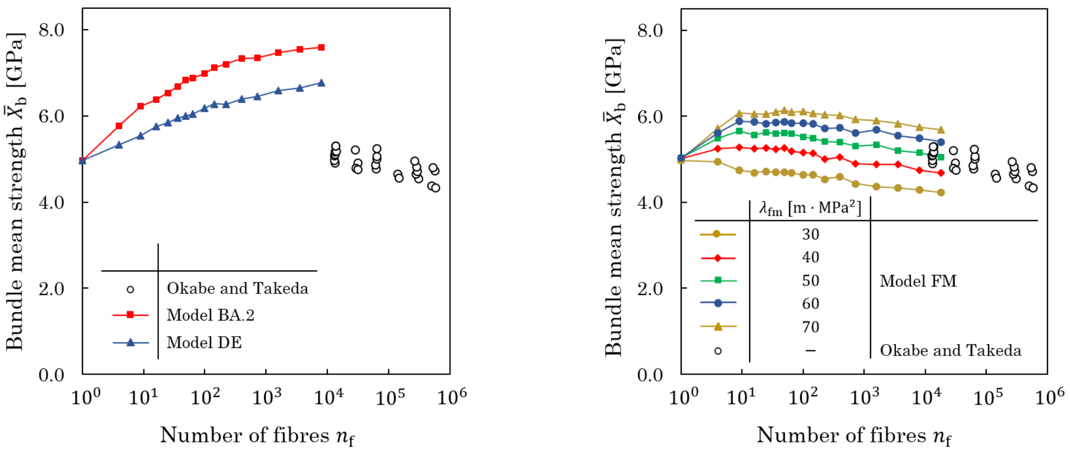

(a)

(b)

Figure 20: Validation of models BA, DE and FM with experimental data of macro-bundles. Results presented for $l_b = 10$ mm. (a) Results for models BA.2 and DE. (b) Results for model FM (with different values of λ_{fm}).

allowing the direct simulation of bundle sizes up to thousands of fibres.

A baseline model (model BA) was developed to reproduce the key features involved in the bundle tensile failure process: variability of single fibre strength and stress concentration around broken fibres. Four sub-variants of the baseline model were created to investigate different aspects of the simulation algorithm (see Table 1). Model BA.1 completely neglects the effect of the cluster size on the fibres recovery length and uses a multiple breaks approach for the simulation algorithm. Model BA.2 still uses the multiple breaks approach but implements an approximate calculation of the stress recovery length for clusters of broken fibres, while model BA.3 implements an exact calculation for the recovery length keeping the multiple breaks approach. Model BA.4 features an exact calculation of the stress recovery length for clusters of broken fibres, but uses a non-simultaneous single fibre failure simulation algorithm (single break approach).

All model BA variants assume strength of materials as the only bundle failure theory, and only consider static stress equilibrium during the simulation. Model DE was developed in order to investigate the effects of dynamic stress concentration on the bundle failure process, while model FM was developed to investigative the effects of including fracture mechanics in the simulation process. To the authors knowledge, it is the first time in the literature that dynamic effects and fracture mechanics are investigated through direct simulation of large composite bundles.

The following conclusions have been reached during the present study:

a) On model BA variants:

- the non-simultaneous fibre failure simulation strategy implemented in Model BA.3 and the multiple fibre failure simulation strategy implemented in model BA.4 are essentially equivalent with regards to the strength prediction, although the multiple breaks approach allows a slight reduction in computational time. To the knowledge of the authors, it is the first systematic comparison of single and multiple breaking approach in a fibre bundle model;
- the comparison between model BA.1, BA.2 and BA.3 demonstrates that the influence of clusters of broken fibres on the stress recovery length has an important effect on the final bundle strength. This effect is captured fully by model BA.3 and with a 5% error by model BA.2. Considering the strong advantage of model BA.2 in terms of computational efficiency, it appears the most appropriate to conduct simulations on large bundle sizes.

b) Models BA.2 and DE show in general a good correlation with experimental strength distributions for micro-bundles of 4 and 7 fibres with two different resin types. Model BA.2 also shows good agreement with Monte Carlo simulations carried out using a full FE bundle model.

c) Model DE, which shares the algorithm of the baseline models but includes the effects of dynamic stress concentrations, shows a maximum reduction possible of about 10% in the predicted bundle strength when compared with model BA.2.

d) Both models BA and DE predict an increase in strength with the bundle size and severely overestimate experimental results, even considering the extreme case scenario for dynamic effects in model DE. These results suggest that there are important aspects of the physics of the problem that are not considered in models BA and DE.

e) Model FM, which shares the same basic algorithm as model BA.2 but includes a fracture mechanics failure criterion, predicts lower bundle strengths and, most importantly, a negative trend for the strength of large bundles in agreement with experimental results. It also predicts a smaller critical cluster size which stays rather constant even for large bundles, in agreement with experimental evidence. These results suggest that fracture mechanics may be the physical mechanism missing in models BA and DE, and that it is necessary to reproduce the size effect in large composite bundles. This is arguably the most important outcome of the work presented in this document.

Acknowledgements

The first, second and fourth authors are grateful to the funding from EPSRC under grant EP/M002500/1. The third author acknowledges the support from the Royal Academy of Engineering for her Research Fellowship on Multiscale discontinuous composites for large scale and sustainable structural applications (20152019).

Appendix A Calculation of the shear-lag stress limit

A.1 Calculation of the shear-lag boundary

At each bundle cross section j, the shear-lag boundary C_{sl}^{ij} is defined for each fibre element ij as the contour over which the load can be transferred. For the set of *intact* elements $\mathbb{N}_{\mathrm{in}}^{j}$ (those with $\sigma_{\mathrm{sl}}^{ij} > \sigma_{\infty}$), $C_{\mathrm{sl}}^{(ij)_{\mathrm{in}}}$ is calculated computing the number of interfaces between ij and other intact elements in the same cross section:

$$C_{\mathrm{sl}}^{(ij)_{\mathrm{in}}} = \frac{C_{\mathrm{f}}}{4} \cdot n_{\mathrm{el,in}}^{ij}, \tag{A1}$$

where $n_{\mathrm{el,in}}^{ij}$ is the number of intact neighbours of the element ij, with a maximum of 4. Fig. A1a illustrates how the shear-lag boundary varies with the available interfaces and the position of the element in the arrangement.

For the set of *saturated* elements $\mathbb{N}_{\mathrm{st}}^{j}$ (those with $\sigma_{\mathrm{sl}}^{ij} \leq \sigma_{\infty}$), the shear-lag boundary may vary if the elements belong to a cluster. Following the definition given in Section 2.2.2, two or more consecutive elements form a cluster in the cross section j if they are saturated, which means that the cross section j is contained into the region of overlap of the recovery lengths corresponding to the fibres to which they belong. The shear-lag boundary for each cluster s in the cross section j containing a set $\mathbb{N}_{\mathrm{cl}}^{sj}$ of $n_{\mathrm{el_{cl}}}^{sj}$ elements is

$$C_{\mathrm{cl}}^{sj} = \frac{C_{\mathrm{f}}}{4} \cdot \sum_{\mathbb{N}_{\mathrm{cl}}^{sj}} n_{\mathrm{el,in}}^{(ij)_{\mathrm{cl}}^{s}}, \tag{A2}$$

where $n_{\mathrm{el,in}}^{(ij)_{\mathrm{cl}}^{s}}$ is the number of intact neighbours of each element $(ij)_{\mathrm{cl}}^{s}$ of the cluster (Fig. A1b). With this formulation, single saturated elements are treated as clusters of size 1.

Since clusters act as stress-lacking regions, all the elements in the same cluster share the same shear-lag boundary. Hence, the individual $C_{\mathrm{sl}}^{(ij)_{\mathrm{cl}}^{s}}$ are calculated:

$$C_{\mathrm{sl}}^{(ij)_{\mathrm{cl}}^{s}} = \frac{C_{\mathrm{cl}}^{sj}}{n_{\mathrm{el_{cl}}}^{sj}}. \tag{A3}$$

A.2 Iterative calculation of the shear-lag stress limit

The calculation of the shear-lag stress limit $\sigma_{\mathrm{sl}}^{ij}$ needs to be performed iteratively, since the interaction between the recovery lengths associated with the different failed elements modifies the shear-lag

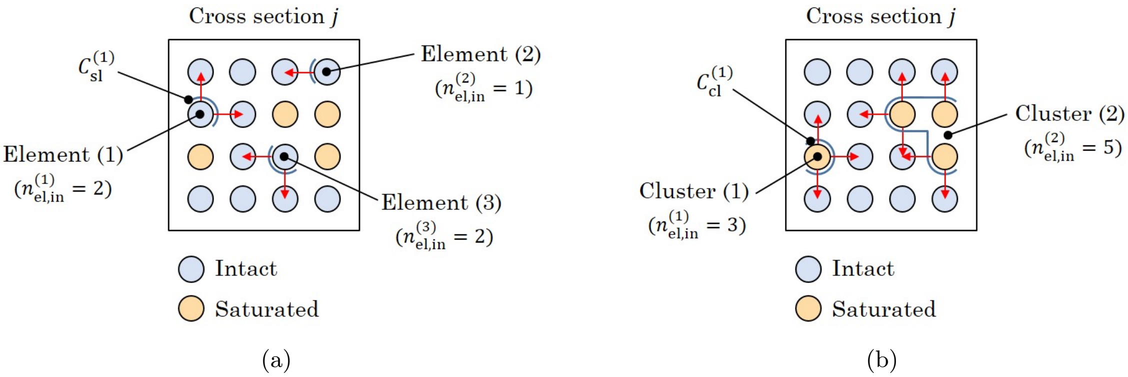

Figure A1: Calculation of shear-lag boundaries in a generic cross section j. (a) Calculation of the shear-lag boundary in three different intact elements. (b) Calculation of the shear-lag boundary in the two clusters with different size.

boundaries C_{sl}^{ij}, and in turn the modification of the boundaries varies the recovery lengths.

To start the iterative process, an initial condition (*initial solution*) for the shear-lag stress limit is firstly calculated. This initial solution does not consider the existence of clusters of broken fibres nor the influence they have in the shear-lag recovery, and it is calculated applying Eqs. (3)-(4) with Eq. (A1) to calculate the shear-lag boundaries. The initial solution is represented with a black line in Fig. A2a. Finally, the set $\mathbb{N}_{\mathrm{st}}$ of saturated elements with $\sigma_{\mathrm{sl}}^{ij} \leq \sigma_{\infty}$ is defined, by computing the individual $\mathbb{N}_{\mathrm{st}}^{j}$ for each cross section j.

At each step, the shear-lag boundary is updated for the set of saturated elements following Eq. (A2)-(A3), and the shear-lag stress limit is re-calculated. Then, the set $\mathbb{N}_{\mathrm{st}}$ is updated to include new saturated elements. The variation of C_{sl}^{ij} in some fibre elements belonging to clusters changes the slope of the shear-lag stress limit profile along the broken fibres, then the recovery lengths change (this effect is highlighted with auxiliary lines in Fig. A2). The solution after the first iterative step is the *simplified shear-lag stress limit*, and it is represented with a red line in Fig. A2a.

When the re-calculation of the shear-lag stress limit does not vary the elements in $\mathbb{N}_{\mathrm{st}}$, the process ends. The solution after completing the iterative process is the *exact shear-lag stress limit* (Fig. A2b).

Appendix B Critical crack size in a unidirectional composite with a centre notch

Composite materials are anisotropic and heterogeneous in nature, and any fracture mechanics analysis should take these factors into account. The problem of predicting the composite failure can

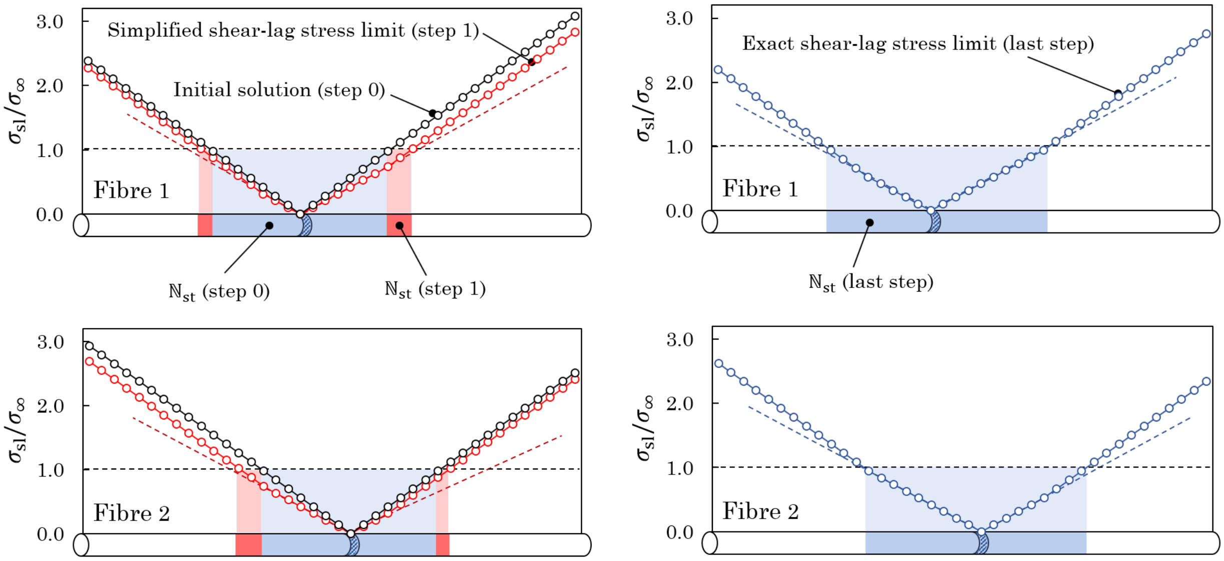

(a) (b)

Figure A2: Calculation of the shear-lag stress limit. (a) First two steps in the calculation of the shear-lag stress limit. The initial solution, which neglects the effect of the cluster, is shown in black and the corresponding set $\mathbb{N}_{\mathrm{st}}$ of the elements included in the recovery lengths is shown in blue. The simplified shear-lag stress limit, which gives a first approximation of the effects of the cluster, and the corresponding set $\mathbb{N}_{\mathrm{st}}$ are shown in red. (b) Converged solution for the calculation of the shear-lag stress limit. The exact solution for shear-lag stress limit and the corresponding set $\mathbb{N}_{\mathrm{st}}$ are shown in blue. In both images, dotted lines are used to highlight the changes in the slope of the shear-lag stress limit when varying C_{sl}^{ij}.

be approached using a critical energy release rate criterion which could describe each specific microstructural failure event. Nairn [58, 67] developed a shear-lag model to find an approximate solution for the stress concentrations around crack tips and around longitudinal splits in unidirectional composites, and used it to calculate the energy release rate due to self-similar crack propagation through the fibres (translaminar crack propagation):

$$G_{\mathrm{T}} = \frac{\sigma_{\infty}^{2} \cdot a}{2 \cdot \sqrt{E_1 \cdot \mu_{12}}} \cdot S_{\mathrm{T}}\left(\frac{a}{W}\right), \tag{A4}$$

and the energy release rate due to longitudinal crack propagation:

$$G_{\mathrm{L}} = \frac{\sigma_{\infty}^{2} \cdot a}{4 \cdot E_1} \cdot S_{\mathrm{L}}\left(\frac{a}{W}, \frac{\Delta}{W}, \sqrt{\frac{\mu_{12}}{E_1}}\right). \tag{A5}$$

In these expressions, a is the crack length, Δ is the longitudinal split length ($\Delta = 0$ for the case of longitudinal splitting from the tip of a crack), E_1 is the composite tensile modulus, μ_{12} is the composite in plane shear modulus, σ_∞ is the asymptotic stress, and L and W are defined in Fig. A3. The functions $S_{\mathrm{T}}(\frac{a}{W})$ and $S_{\mathrm{L}}(\frac{a}{W},\ \frac{\Delta}{W},\ \sqrt{\frac{\mu_{12}}{E_1}})$ are the finite width corrections factors and tend to π for infinite samples (the methods for calculating them are detailed in [58]).

The energy release rate expressions in Eqs. (A4) and (A5) can be combined and re-arranged to calculate the critical crack length a_{cr}:

$$a_{\mathrm{cr}} = \min\left(\frac{2\cdot\sqrt{E_1\cdot\mu_{12}}\cdot G_{\mathrm{Tc}}}{\sigma_\infty^2\cdot S_{\mathrm{T}}},\ \frac{4\cdot E_1\cdot G_{\mathrm{Lc}}}{\sigma_\infty^2\cdot S_{\mathrm{L}}}\right), \tag{A6}$$

where G_{Tc} and G_{Lc} are the critical energy release rates for translaminar and longitudinal crack propagation respectively.

The fracture mechanics failure criterion expressed in Eq. (A6) can be further synthesized in the form:

$$a_{\mathrm{cr}} = \frac{\lambda_{\mathrm{fm}}}{\sigma_\infty^2}, \tag{A7}$$

where λ_{fm} is a proportionality factor which includes geometric effects as well as materials properties information and is given by:

$$\lambda_{\mathrm{fm}} = \min\left(\lambda_{\mathrm{fm}}^{\mathrm{T}}, \lambda_{\mathrm{fm}}^{\mathrm{L}}\right), \quad \text{with} \tag{A8}$$

$$\lambda_{\mathrm{fm}}^{\mathrm{T}} = \frac{2\cdot\sqrt{E_1\cdot\mu_{12}}\cdot G_{\mathrm{Tc}}}{S_{\mathrm{T}}}, \quad \text{and} \tag{A9}$$

$$\lambda_{\mathrm{fm}}^{\mathrm{L}} = \frac{4\cdot E_1\cdot G_{\mathrm{Lc}}}{S_{\mathrm{L}}}. \tag{A10}$$

Appendix C Numerical convergence study

This section summarizes the convergence study conducted to select the appropriate numerical parameters for the simulations. The study was performed using the model BA.4 with a bundle length $l_{\mathrm{s}} = l_{\mathrm{b}} = 1$ mm and the nominal geometrical and mechanical properties listed in Table 2.

Fig. A4a shows the predicted mean strength and variability for different levels of bundle discretization (varying the element length l_{el}), with a constant size for the confidence interval of the mean strength (with $e_{\bar{\mathrm{X}}} = \pm 1\%$). The model appears to reach convergence for the range of element sizes simulated, although both the strength and variability curves show small residual fluctuations. This effect is attributed to the stochastic nature of the simulation, rather than to the discretization level,

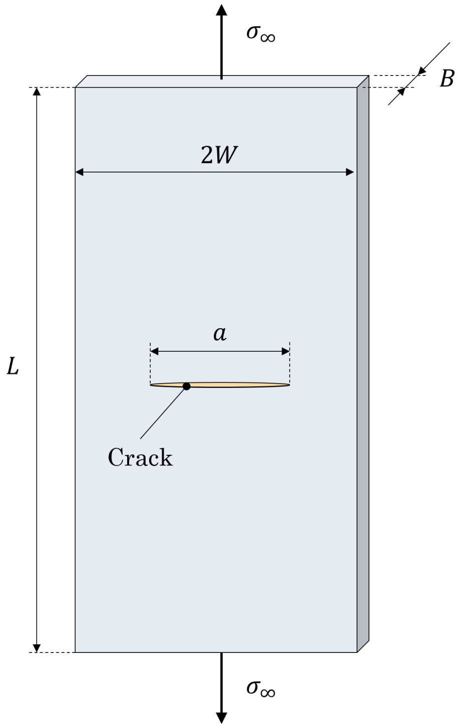

Figure A3: Centre notch crack in a unidirectional composite sample.

and therefore is more likely to be affected by the required precision of the Monte Carlo simulation, which is discussed below.

Fig. A4b shows that the number of Monte Carlo simulations was roughly the same for all the element sizes, and the computational cost is a direct function of the average time per simulation, which increases by 20 times when decreasing l_{el} from 0.05 mm to $l_{\mathrm{el}} = 0.001$ mm. An element size $l_{\mathrm{el}} = 0.005$ mm is used for all the simulations in Section 3 to ensure a good compromise between precision and computational efficiency.

Fig. A4c-d show the results of varying the size of the confidence interval for the mean strength $\bar{X}_{\mathrm{b}}$ in Eq. (10), while keeping the level of discretization constant ($l_{\mathrm{el}} = 0.005$ mm). Decreasing the size of the confidence interval decreases the random fluctuation in the results, particularly for the coefficient of variation, but also produces a strong increase in the required number of Monte Carlo simulations (Fig. A4d). A maximum accepted error $e_{\bar{\mathrm{X}}} = \pm 1\%$ (see Section 2.2.5) produces reliable results with good performances regarding computational time, and is used for all the simulations in Section 3.

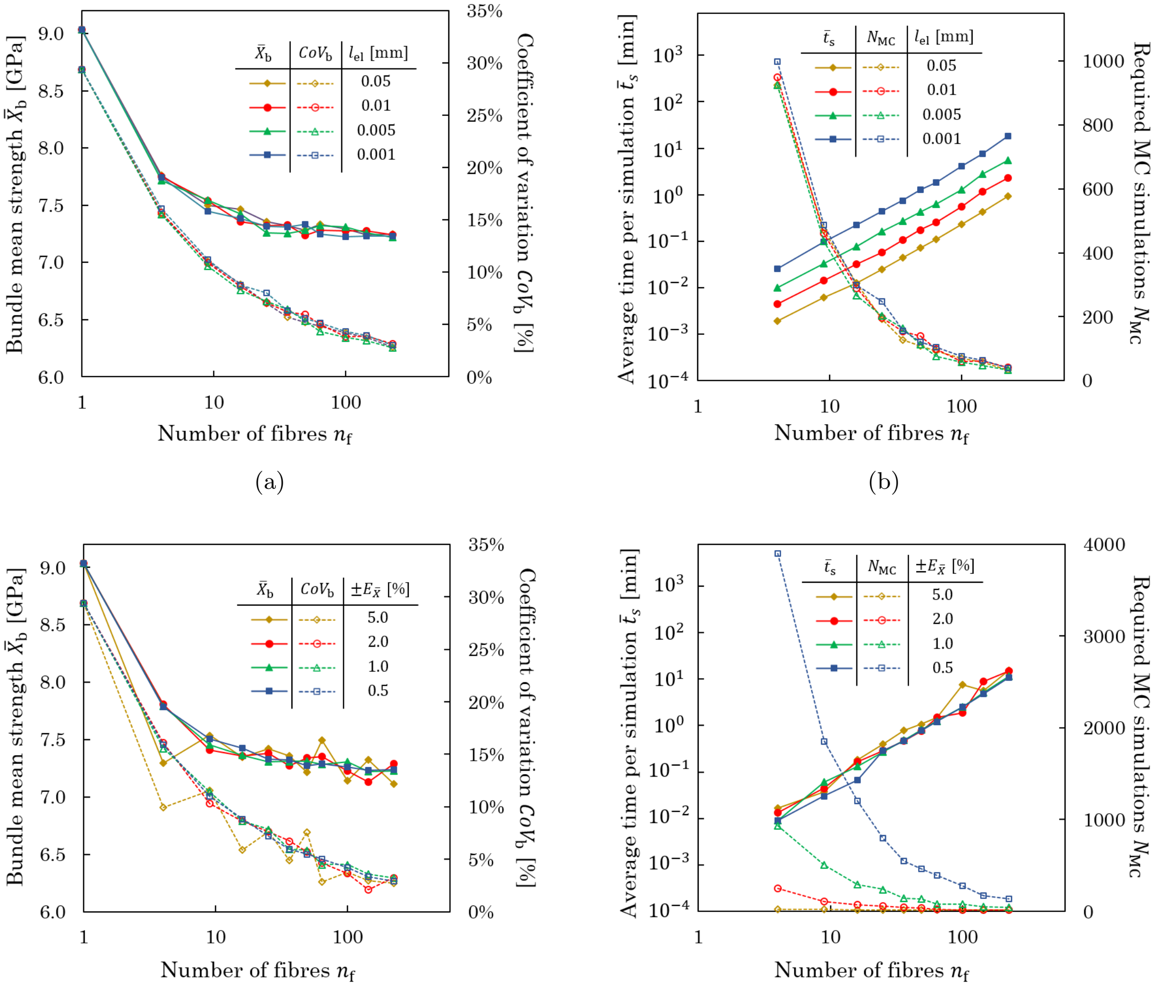

(a)

(b)

(c)

(d)

Figure A4: Numerical convergence study. (a) Comparison of mean strength and coefficient of variation for different discretization levels (variation of l_{el}). (b) Computational cost for different discretization levels. (c) Comparison of mean strength and coefficient of variation for different sizes of the confidence interval for $\bar{X}_b$ (variation of $E_{\bar{X}}$). (d) Computational cost for different sizes of the confidence interval for $\bar{X}_b$.

Appendix D Length scaling

To improve computational efficiency, strength results for large fibre bundles (with true length l_b) are obtained by simulating a bundle model with the same number of fibres and a representative bundle length $l_s < l_b$. The simulation results are then scaled to the true bundle length applying the Weakest Link Theory (WLT) [8, 43], which states that a chain of length l_n composed by n elements of length l_0 survives under a remote stress σ_∞ only if each of the elements survives under σ_∞. Hence, the failure probability $F_b(\sigma_\infty)$ (or strength cumulative distribution function) for a bundle of length l_b is

$$F_\mathrm{b}(\sigma_\infty) = 1 - [1 - F_\mathrm{s}(\sigma_\infty)]^{l_\mathrm{b}/l_\mathrm{s}}, \tag{A11}$$

where $F_\mathrm{s}(\sigma_\infty)$ is the failure probability for a bundle of length l_s under the remote stress σ_∞, which can be obtained directly from the simulation.

Two different scaling methods are implemented: (i) scaling the strength distribution directly, or (ii) scaling the statistical parameters of the distribution. In case (i), being $X_\mathrm{b}^1 \leq X_\mathrm{b}^2 \leq ... \leq X_\mathrm{b}^N ... \leq X_\mathrm{b}^{N_\mathrm{MC}}$ the predicted bundle strengths corresponding to each one of the N_MC Monte Carlo simulations for a bundle of length l_s, the value of the failure probability is assigned to each strength value following

$$F_\mathrm{s}^N = (N-1)/N_\mathrm{MC}, \tag{A12}$$

and then $F_\mathrm{b}^{N_\mathrm{MC}}$ is calculated applying Eq. (A11).

In case (ii), the predicted strength distribution for each simulated bundle with length l_s is fitted using a Weibull distribution with parameters m^s and X_0^s that correspond to the mean bundle strength $\bar{X}_\mathrm{b}^\mathrm{s}$ and standard deviation SD_b^s. These parameters are then scaled to l_b using WLT:

$$\begin{aligned} m^\mathrm{b} &= m^\mathrm{s} \\ X_0^\mathrm{b} &= X_0^\mathrm{s} \left(\frac{l_\mathrm{s}}{l_\mathrm{b}}\right)^{1/m^\mathrm{s}} \end{aligned} \tag{A13}$$

Since, in general, the accuracy of the Monte Carlo simulation tends to converge much faster for the mean strength than for the standard deviation, using the latter (option (ii)) to perform the scaling may introduce artificial noise in the scaled results for the mean strength. For these reasons the curve $SD_\mathrm{b}^\mathrm{s}(n_\mathrm{f})$ is fitted with a power law $c_1 \cdot (n_\mathrm{f})^{c_2}$ before applying the scaling to smooth random fluctuations related to the convergence of the Monte Carlo simulations.

Fig. A5 shows an overview of the different scaling approaches. The model BA.4 was used with the nominal inputs from Table 2. Fig. A5a presents the mean strength and variability for different simulation lengths l_s, while Fig. A5b-c show the same results scaled to $l_\mathrm{b} = 5$ mm using methods (i), and (ii) respectively, and compare them with the non-scaled solution ($l_\mathrm{s} = l_\mathrm{b}$).

Scaling the entire distribution (Fig. A5b) may overestimate slightly the strength; this is because Eq. (A11) causes loss of accuracy in the lower tail of the distribution. On the contrary, scaling the statistical parameters leads to a better prediction of the mean strength, especially if the standard deviation is fitted (Fig. A5c). Therefore, scaling technique (ii) with fitting the standard deviation has been mainly used throughout this document.

Finally, it is important to observe that, for bundles with length $l_b = 5$ mm, both the simulated results and the scaled results predict an upward trend of the mean bundle strength with the bundle size. Thus, this is not an artefact of the scaling technique but an actual result of the model.

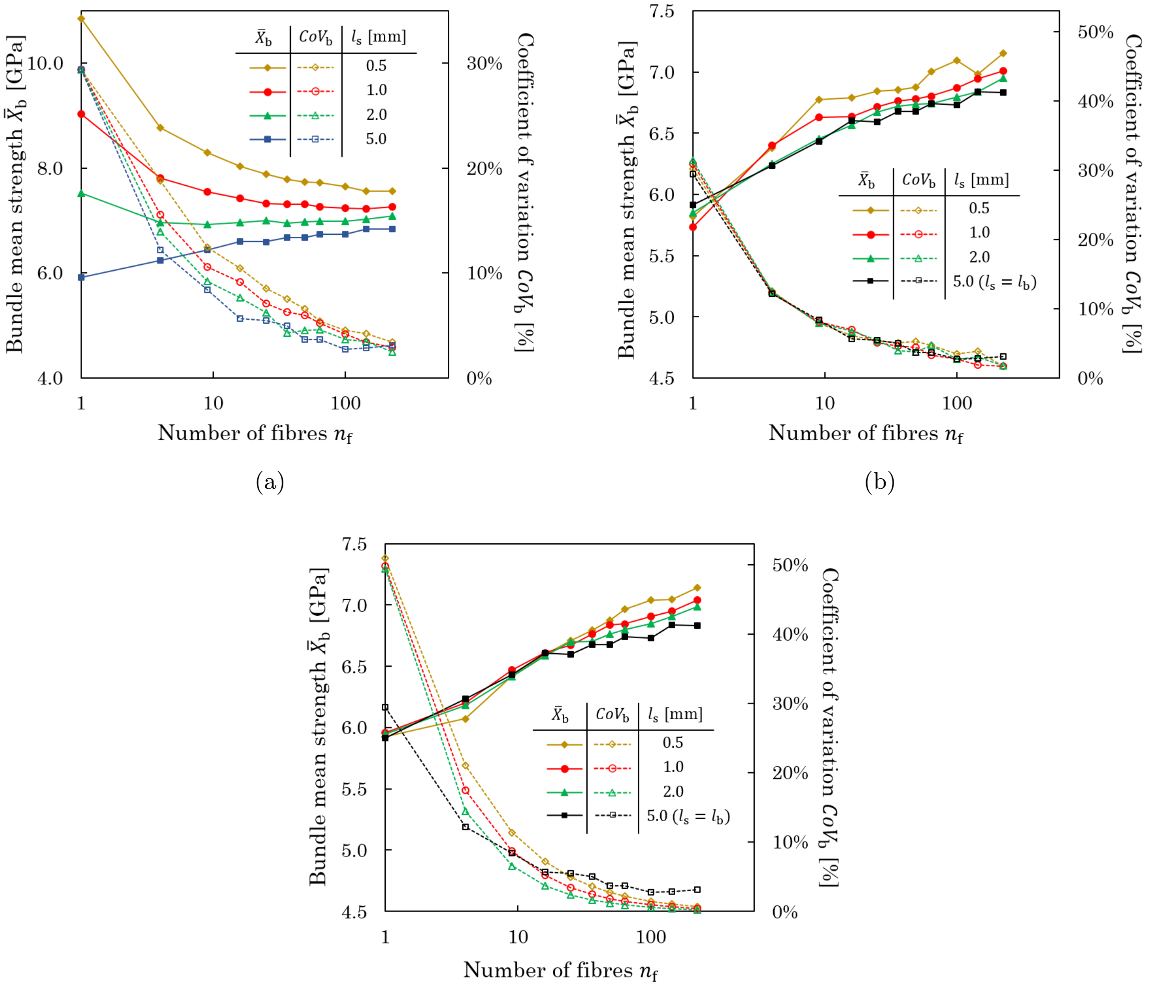

(a)

(b)

(c)

Figure A5: Length scaling. (a) Comparison of mean strength and coefficient of variation for different simulations lengths. (b) Results for $l_b = 5$ mm scaling the entire distribution. (c) Results for $l_b = 5$ mm scaling the statistical parameters with fitting the standard deviation.

Appendix E Implementation of Weibull of Weibull distribution for the fibre elements strength

To model the stochastic variability of the fibre strength following a Weibull of Weibull distribution [5], a random strength X^{ij} is assigned to each fibre element in the bundle following

$$F_{\mathrm{el}}(X^{ij}) = 1 - \exp\left(-\frac{X^{ij}}{X_0^{l_{\mathrm{el}},i}}\right)^{\rho_1}, \tag{A14}$$

where ρ_1 and $X_0^{l_{\mathrm{el}},i}$ are the shape and scale parameters, respectively, for the strength distribution of an element of length l_{el} which belongs to fibre i. The scale parameter $X_0^{l_{\mathrm{el}},i}$ changes from fibre to fibre in the bundle following a second Weibull distribution

$$F_{\mathrm{el}}(X_0^{l_{\mathrm{el}},i}) = 1 - \exp\big[-\frac{l_{\mathrm{el}}}{l_{\mathrm{r}}}\left(\frac{X_0^{l_{\mathrm{el}},i}}{\bar{X}_0^{l_{\mathrm{r}}}}\right)^{\rho_2}\big], \tag{A15}$$

where $\bar{X}_0^{l_{\mathrm{r}}}$ and ρ_2 are the scale and shape parameters, respectively, for a fibre of reference length l_{r}.

References

[1] M R Wisnom. Size effects in the testing of fibre-composite materials. *Compos. Sci. Technol.*, 59(13):1937–1957, 1 October 1999.

[2] X Xu, M R Wisnom, Y Mahadik, and S R Hallett. An experimental investigation into size effects in quasi-isotropic carbon/epoxy laminates with sharp and blunt notches. *Compos. Sci. Technol.*, 100:220–227, 21 August 2014.

[3] X Xu, M R Wisnom, X Li, and S R Hallett. A numerical investigation into size effects in centre-notched quasi-isotropic carbon/epoxy laminates. *Compos. Sci. Technol.*, 111:32–39, 6 May 2015.

[4] Z P Bažant. Size effect on structural strength: a review. *Arch. Appl. Mech.*, 69(9-10):703–725, 1 November 1999.

[5] T Okabe. Size effect on tensile strength of unidirectional CFRP composites— experiment and simulation. *Compos. Sci. Technol.*, 62(15):2053–2064, 2002.

[6] M R Wisnom, B Khan, and S R Hallett. Size effects in unnotched tensile strength of unidirectional and quasi-isotropic carbon/epoxy composites. *Compos. Struct.*, 84(1):21–28, 1 June 2008.

[7] Y Swolfs, S Pimenta, A Thionnet, A Bunsell, L Gorbatikh, H Morton, I Sinclair, and M Spearing. A benchmarking exercise for three longitudinal strength models for unidirectional fibre-reinforced composites. *Proceedings of ICCM-21. Xi'an, China*, 2017.

[8] S Pimenta. Fibre failure modelling. In P P Camanho and S R Hallett, editors, *Numerical Modelling of Failure in Advanced Composite Materials*, pages 193–224. 2015.

[9] Y Swolfs, I Verpoest, and L Gorbatikh. A review of input data and modelling assumptions in longitudinal strength models for unidirectional fibre-reinforced composites. *Compos. Struct.*, 150:153–172, 15 August 2016.

[10] I J Beyerlein and S L Phoenix. Stress concentrations around multiple fiber breaks in an elastic matrix with local yielding or debonding using quadratic influence superposition. *J. Mech. Phys. Solids*, 44(12):1997–2039, 1996.

[11] C M Landis, I J Beyerlein, and R M McMeeking. Micromechanical simulation of the failure of fiber reinforced composites. *J. Mech. Phys. Solids*, 48(3):621–648, 2000.

[12] I J Beyerlin and S L Phoenix. Statistics of fracture for an elastic notched composite lamina containing weibull fibers part II. probability models of crack growth. *Eng. Fract. Mech.*, 57(2–3):267–299, 1997.

[13] W A Curtin and N Takeda. Tensile strength of Fiber-Reinforced composites: I. model and effects of local fiber geometry. *J. Compos. Mater.*, 32(22):2042–2059, 1 November 1998.

[14] M Ibnabdeljalil and W A Curtin. Strength and reliability of fiber-reinforced composites: Localized load-sharing and associated size effects. *Int. J. Solids Struct.*, 34(21):2649–2668, 1997.

[15] B W Rosen. Tensile failure of fibrous composites. *AIAA JOURNAL*, 2(11):1985–1991, 1964.

[16] W A Curtin. Theory of mechanical properties of Ceramic-Matrix composites. *J. Am. Ceram. Soc.*, 74(11):2837–2845, 1 November 1991.

[17] H E Daniels. The statistical theory of the strength of bundles of threads I. *NATO Adv. Sci. Inst. Ser. C Math. Phys. Sci.*, 183:405–435, 1945.

[18] J M Hedgepeth. Stress concentrations in filamentary structures. *NASA technical report*, 1 May 1961.

[19] D G Harlow and S L Phoenix. The Chain-of-Bundles probability model for the strength of fibrous materials i: Analysis and conjectures. *J. Compos. Mater.*, 12(2):195–214, 1 July 1978.

[20] D G Harlow and S L Phoenix. The Chain-of-Bundles probability model for the strength of fibrous materials II: A numerical study of convergence. *J. Compos. Mater.*, 12(3):314–334, 1 October 1978.

[21] S J Zhou and W A Curtin. Failure of fiber composites: A lattice green function model. *Acta Metall. Mater.*, 43(8):3093–3104, 1995.

[22] L St-Pierre, N J Martorell, and S T Pinho. Stress redistribution around clusters of broken fibres in a composite. *Compos. Struct.*, 168:226–233, 15 May 2017.

[23] A Thionnet, H Y Chou, and A Bunsell. Fibre break failure processes in unidirectional composites. part 1: Failure and critical damage state induced by increasing tensile loading. *Appl. Compos. Mater.*, 22(2):119–140, 1 April 2015.

[24] A Thionnet, H Y Chou, and A Bunsell. Fibre break processes in unidirectional composites. *Compos. Part A Appl. Sci. Manuf.*, 65:148–160, October 2014.

[25] S Blassiau, A Thionnet, and A R Bunsell. Three-dimensional analysis of load transfer micromechanisms in fibre/matrix composites. *Compos. Sci. Technol.*, 69(1):33–39, 2009.

[26] T Okabe, N Takeda, Y Kamoshida, M Shimizu, and W A Curtin. A 3d shear-lag model considering micro-damage and statistical strength prediction of unidirectional fiber-reinforced composites. *Compos. Sci. Technol.*, 61(12):1773–1787, 2001.

[27] T Okabe, H Sekine, K Ishii, M Nishikawa, and N Takeda. Numerical method for failure simulation of unidirectional fiber-reinforced composites with spring element model. *Compos. Sci. Technol.*, 65(6):921–933, 2005.

[28] Y Swolfs, R M McMeeking, I Verpoest, and L Gorbatikh. Matrix cracks around fibre breaks and their effect on stress redistribution and failure development in unidirectional composites. *Compos. Sci. Technol.*, 108:16–22, 2015.

[29] S Pimenta and S T Pinho. Hierarchical scaling law for the strength of composite fibre bundles. *J. Mech. Phys. Solids*, 61(6):1337–1356, 2013.

[30] Z Xia, W A Curtin, and T Okabe. Green's function vs. shear-lag models of damage and failure in fiber composites. *Compos. Sci. Technol.*, 62(10-11):1279–1288, 2002.

[31] Z P Bazant, I M Daniel, and Z Li. Size effect and fracture characteristics of composite laminates. *of the ASME)(* , 1996.

[32] S Pimenta and P Robinson. An analytical model for the mechanical response of discontinuous composites. *Proceedings of ICCM-19. Montreal, Canada*, 2013.

[33] J Henry and S Pimenta. Semi-analytical simulation of aligned discontinuous composites. *Compos. Sci. Technol.*, 144(Supplement C):230–244, 26 May 2017.

[34] D Raz-Ben Aroush, E Maire, C Gauthier, S Youssef, P Cloetens, and H D Wagner. A study of fracture of unidirectional composites using in situ high-resolution synchrotron x-ray microtomography. *Compos. Sci. Technol.*, 66(10):1348–1353, 1 August 2006.

[35] A E Scott, M Mavrogordato, P Wright, I Sinclair, and S M Spearing. In situ fibre fracture measurement in carbon–epoxy laminates using high resolution computed tomography. *Compos. Sci. Technol.*, 71(12):1471–1477, 19 August 2011.

[36] E N Sakharova and A S Ovchinskii. Dynamics of stress redistribution in a ruptured fiber of a composition material. *Mech. Compos. Mater.*, 15(1):45–51, 1 January 1979.

[37] R Ganesh, S Sockalingam, B Z (Gama) Haque, and J W Gillespie. Dynamic effects of single fiber break in unidirectional glass fiber-reinforced composites. *J. Compos. Mater.*, 51(9):1307–1320, 15 September 2016.

[38] E N Sakharova and A S Ovchinskii. Influence of dynamic effects accompanying rupture of fibers and separation of fibers from the matrix on interaction between failure micromechanisms of composite materials. *Mech. Compos. Mater.*, 20(3):323–327, 1 May 1984.

[39] J Xing, X R Liu, and T W Chou. Dynamic stress concentration factors in unidirectional composites. *J. Compos. Mater.*, 19(3):269–275, 1 May 1985.

[40] G B Bullegas and J M Lamela. Semi-analytical fibre bundle model. https://github.com/Gianbullegas/SemiAnalytical-FibreBundle-Strength, 2019.

[41] V Romanov, S V Lomov, Y Swolfs, S Orlova, L Gorbatikh, and I Verpoest. Statistical analysis of real and simulated fibre arrangements in unidirectional composites. *Compos. Sci. Technol.*, 87(Supplement C):126–134, 18 October 2013.

[42] G W Weibull. A statistical distribution function of wide applicability. *J. Appl. Math.*, pages 293–297, 1951.

[43] F T Peirce. Tensile tests for cotton yarns:“the weakest link” theorems on the strength of long and of composite specimens. *J. Text. Inst.*, 17:T355–368, 1926.

[44] Y Swolfs, I Verpoest, and L Gorbatikh. Issues in strength models for unidirectional fibre-reinforced composites related to weibull distributions, fibre packings and boundary effects. *Compos. Sci. Technol.*, 114(Supplement C):42–49, 19 June 2015.

[45] Y Swolfs, H Morton, A E Scott, L Gorbatikh, P A S Reed, I Sinclair, S M Spearing, and I Verpoest. Synchrotron radiation computed tomography for experimental validation of a tensile strength model for unidirectional fibre-reinforced composites. *Compos. Part A Appl. Sci. Manuf.*, 77(Supplement C):106–113, 1 October 2015.

[46] Y Swolfs, R M McMeeking, I Verpoest, and L Gorbatikh. The effect of fibre dispersion on initial failure strain and cluster development in unidirectional carbon/glass hybrid composites. *Compos. Part A Appl. Sci. Manuf.*, 69(Supplement C):279–287, 1 February 2015.

[47] S Pimenta and S T Pinho. An analytical model for the translaminar fracture toughness of fibre composites with stochastic quasi-fractal fracture surfaces. *J. Mech. Phys. Solids*, 66(1):78–102, 2014.

[48] T Okabe, M Nishikawa, N Takeda, and H Sekine. Effect of matrix hardening on the tensile strength of alumina fiber-reinforced aluminum matrix composites. *Acta Mater.*, 54(9):2557–2566, 1 May 2006.

[49] P T Curtis. A computer model of the tensile failure process in unidirectional fibre composites. *Compos. Sci. Technol.*, 27:63–86, 1986.

[50] I J Beyerlein and S L Phoenix. Statistics for the strength and size effects of microcomposites with four carbon fibers in epoxy resin. *Compos. Sci. Technol.*, 56(1):75–92, 1 January 1996.

[51] M Kazanci. Carbon fiber reinforced microcomposites in two different epoxies. *Polym. Test.*, 23(7):747–753, 1 October 2004.

[52] R Gulino and S L Phoenix. Weibull strength statistics for graphite fibres measured from the break progression in a model graphite/glass/epoxy microcomposite. *J. Mater. Sci.*, 26(11):3107–3118, 1 June 1991.

[53] J Watanabe, F Tanaka, H Okuda, and T Okabe. Tensile strength distribution of carbon fibers at short gauge lengths. *Adv. Compos. Mater.*, 23(5-6):535–550, 3 September 2014.

[54] J Yao, W Yu, and D Pan. Tensile strength and its variation of PAN-based carbon fibers. III. weak-link analysis. *J. Appl. Polym. Sci.*, 110(6):3778–3784, 15 December 2008.

[55] A Kelly and W R Tyson. Tensile properties of fibre-reinforced metals: Copper/tungsten and copper/molybdenum. *J. Mech. Phys. Solids*, 13(6):329–350, 1 December 1965.

[56] C M Landis and R M McMeeking. A shear-lag model for a broken fiber embedded in a composite with a ductile matrix. *Compos. Sci. Technol.*, 59(3):447–457, 1 February 1999.

[57] R C Hidalgo, Y Moreno, F Kun, and H J Herrmann. Fracture model with variable range of interaction. *Phys. Rev. E*, 65(4):046148/1–046148/8, 2002.

[58] J A Nairn. Fracture mechanics of unidirectional composites using the Shear-Lag model i: Theory. *J. Compos. Mater.*, 22(6):561–588, June 1988.

[59] A. Sapora, P. Cornetti, A. Carpinteri, and D. Firrao. Brittle materials and stress concentrations: are they able to withstand? *Procedia Engineering*, 109:296 – 302, 2015.

[60] M.R. Ayatollahi and A.R. Torabi. Brittle fracture in rounded-tip v-shaped notches. *Materials Design*, 31(1):60 – 67, 2010.

[61] D. Taylor. Predicting the fracture strength of ceramic materials using the theory of critical distances. *Engineering Fracture Mechanics*, 71(16):2407 – 2416, 2004.

[62] A N Netravali, R B Henstenburg, S L Phoenix, and P Schwartz. Interfacial shear strength studies using the single-filament-composite test. i: Experiments on graphite fibers in epoxy. *Polym. Compos.*, 10(4):226–241, 1989.

[63] R F Teixeira, S T Pinho, and P Robinson. Thickness-dependence of the translaminar fracture toughness: Experimental study using thin-ply composites. *Compos. Part A Appl. Sci. Manuf.*, 90:33–44, 2016.

[64] Kuniaki Honjo. Fracture toughness of PAN-based carbon fibers estimated from strength-mirror size relation. *Carbon N. Y.*, 41(5):979–984, 2003.

[65] M J Laffan, S T Pinho, P Robinson, and L Iannucci. Measurement of the in situ ply fracture toughness associated with mode I fibre tensile failure in FRP. part I: Data reduction. *Compos. Sci. Technol.*, 70(4):606–613, 2010.

[66] M J Laffan, S T Pinho, P Robinson, and L Iannucci. Measurement of the in situ ply fracture toughness associated with mode I fibre tensile failure in FRP. part II: Size and lay-up effects. *Compos. Sci. Technol.*, 70(4):614–621, 1 2010.

[67] J A Nairn. Fracture mechanics of unidirectional composites using the Shear-Lag model II: Experiment. *J. Compos. Mater.*, 22(6):589–600, June 1988.